Wulf, H., Bookhagen, B., Scherler, D. (2016): Differentiating between rain, snow, and glacier contributions to river discharge in the western Himalaya using remote-sensing data and distributed hydrological modeling. - *Advances in Water Resources*, *88*, pp. 152—169.

DOI: http://doi.org/10.1016/j.advwatres.2015.12.004

# Differentiating between rain, snow, and glacier contributions to river discharge in the western Himalaya using remote-sensing data and distributed hydrological modeling

Hendrik Wulf [1,2], Bodo Bookhagen [1,3], Dirk Scherler [1,4,5]

[1] Department of Earth and Environmental Science, Potsdam University, Germany

[2] now at: Remote Sensing Laboratories, Department of Geography, University of Zurich, Zurich, Switzerland

[3] Department of Geography, University of California, Santa Barbara, USA

[4] Earth Surface Geochemistry, Helmholtz Centre Potsdam, GFZ German Research Center for Geosciences, Telegrafenberg, 14473 Potsdam, Germany

[5] Institute of Geological Sciences, Freie Universität Berlin, 12249 Berlin, Germany

Correspondence to: H. Wulf (hendrik.wulf@geo.uzh.ch)

**Index Terms:** 1860, 1847, 1863, 1854, 1855

**Keywords:** runoff modeling, MODIS, TRMM, mountain hydrology, Sutlej River

**Key points:**

- Rainfall (55%) and snow- and glacier melt (45%) contribute approximately equally to Sutlej River discharge
- Glacier melt accounts for one third in river discharge in the Himalayan interior
- The TRMM 3B42 product overestimates rainfall in the arid orogenic interor

## Abstract

Rivers draining the southern Himalaya provide most of the water supply for the densely populated Indo-Gangetic plains. Despite the importance of water resources in light of climate change, the relative contributions of rainfall, snow and glacier melt to discharge are not well understood, due to the scarcity of ground-based data in this complex terrain. Here, we quantify discharge sources in the Sutlej Valley, western Himalaya, from 2000 to 2012 with a distributed hydrological model that is based on daily, ground-calibrated remote-sensing observation. Based on the consistently good model performance, we analyzed the spatiotemporal distribution of hydrologic components and quantified their contribution to river discharge. Our results indicate that the Sutlej River's annual discharge at the mountain front is sourced to 55% by effective rainfall (rainfall reduced by evapotranspiration), 35% by snow melt and 10% by glacier melt. In the high-elevation orogenic interior glacial runoff contributes ~30% to annual river discharge. These glacier melt contributions are especially important during years with substantially reduced rainfall and snowmelt runoff, as during 2004, to compensate for low river discharge and ensure sustained water supply and hydropower generation. In 2004, discharge of the Sutlej River totaled only half the maximum annual discharge; with 17.3% being sourced by glacier melt. Our findings underscore the importance of calibrating remote-sensing data with ground-based data to constrain hydrological models with reasonable accuracy. For instance, we found that TRMM (Tropical Rainfall Measuring Mission) product 3B42 V7 systematically overestimates rainfall in arid regions of our study area by a factor of up to 5. By quantifying the spatiotemporal distribution of water resources we provide an important assessment of the potential impact of global warming on river discharge in the western Himalaya. Given the near-global coverage of the utilized remote-sensing datasets this hydrological modeling approach can be readily transferred to other data-sparse regions.

# 1 Introduction

Runoff from the Himalaya is extensively used for hydropower generation, agriculture, as well as urban and rural household use in the densely populated Indo-Gangetic Plains [*Barnett et al.*, 2005; *Bookhagen and Burbank*, 2010]. In light of recent climatic change [*IPCC,* 2014], glacial retreat [*Bhambri and Bolch*, 2009; *Scherler et al.*, 2011; *Sorg et al.*, 2012], population growth [*WDI*, 2010] and groundwater depletion [*Rodell et al.*, 2009] quantitative assessment of the available water resources in this region is a crucial task [*Immerzeel et al.*, 2010; *Zhang et al.*, 2013]. Although discharge generated from melting of snow and ice is generally assumed to be significant, the scarcity of detailed ground-based observations make quantification of their relative contributions to Himalayan discharge difficult.

Hydrological models are useful tools to explore and quantify fluvial discharge. Runoff from melting snow and ice is commonly estimated using either surface-energy balance [*Anderson*, 1976; *Jin et al.*, 1999] or temperature-index models [*Lang and Braun*, 1990; *Martinec*, 1975; *Rango and Martinec*, 1995]. In the Himalayan region, large-scale surface-energy balance approaches are currently not feasible, because of poorly validated input variables (e.g., wind speed, water-vapor pressure, humidity, radiation fluxes, etc.). In contrast, temperature-index models, which represent simplified empirically based alternatives, require less input data that are usually available for most regions on Earth. However, their simplicity may lead to lower accuracy and larger uncertainties of the results [*Franz et al.*, 2010; *Pellicciotti et al.*, 2005; *Ragettli et al.*, 2013]. Furthermore, coefficients of temperature-index models can vary significantly within individual watersheds [*He et al.*, 2014; *Kumar et al.*, 2013]. For a stronger physical basis of the melt water generation, the shortwave radiation balances can be included in so-called *enhanced* temperature-index models [*Hock*, 1999; *Pellicciotti et al.*, 2005; *Rango and Martinec*, 1995]. Furthermore, spatially distributed models are able to account for the high spatial variability of meteorological parameters in mountain regions

73 [*Gurtz et al.*, 1999], but require input data that approximately match the spatial resolution of
74 the model grid.

75 To achieve complete input data coverage in distributed models, previous studies have
76 commonly extrapolated low-elevation station data to higher altitudes [e.g. *Braun et al.*, 1993;
77 *Li and Williams*, 2008; *Singh and Jain*, 2002; *Singh and Bengtsson*, 2003]. Extrapolation of
78 station data for catchments with a high elevation range is problematic in mountainous regions
79 because of the high spatial variability of both, precipitation and temperature [*Barros et al.*,
80 2004; *Bookhagen and Burbank*, 2006; *Lundquist and Cayan*, 2007]. Alternatively, several
81 satellite systems provide processed and gridded data products that can be used for
82 hydrological modeling [*Bales et al.*, 2006; *Schmugge et al.*, 2002]. In the Himalaya, various
83 MODIS and TRMM data products have been successfully integrated in hydrological models
84 by studies that focused on mean-monthly discharges [e.g., *Bookhagen and Burbank*, 2010], or
85 daily discharges in very large watersheds using MODIS [e.g., *Immerzeel et al.*, 2009]. Such
86 approaches take advantage of temporal and/or spatial averaging, which reduces the
87 uncertainties in the remote-sensing input data that typically contain noise, artifacts, and data
88 gaps introduced by varying surface and atmospheric conditions, as well as specific sensor
89 characteristics and data-processing methods [*Dozier et al.*, 2008]. Therefore, hydrological
90 models with a high spatial and temporal resolution using remote-sensing based information on
91 water fluxes (e.g. rainfall, evaporation) or land cover (e.g. snow cover, vegetation) need to be
92 carefully calibrated to account for these uncertainties.

93 Recent hydrological modeling studies indicate high snow melt contributions to river discharge
94 in the western Himalaya on the order of 30% to 60% [*Bookhagen and Burbank*, 2010;
95 *Immerzeel et al.*, 2009; *Jeelani et al.*, 2012; *Singh and Jain*, 2002]. In contrast, estimates of
96 glacier melt contributions to river discharge in the Himalaya vary considerably between 2% to
97 30%, depending mainly on differences in glacierized catchment area, precipitation,

98 temperature, and solar radiation [*Alford and Armstrong*, 2010; *Immerzeel et al.*, 2009; *Jeelani*
99 *et al.*, 2012; *Racoviteanu et al.*, 2013].

100 The objective of this study is to develop a distributed hydrological model that is driven by
101 calibrated remote-sensing data to study discharges in variably-sized catchments in steep
102 mountainous regions, where ground-based stations are rare. As part of our modeling effort,
103 we assess to what degree calibrated remotely sensed data change the model results, when
104 compared to simple extrapolation of station data and uncalibrated remote-sensing data. Based
105 on the hydrological model we analyze the spatial distribution of water resources and the
106 temporal variations of river discharge components in the Sutlej Valley for the study period
107 from 2000 to 2012. Furthermore, we investigate the relation of glacier snow-cover periods
108 and glacier melt. Based on our novel approach to drive a distributed hydrological model with
109 calibrated remote sensing data, we are able to accurately quantify the spatial and temporal
110 variations in the release of transient water storages and investigate their impact on river
111 discharge.

112 ## 2 Study area

113 The Sutlej River is a tributary of the Indus River and has the third largest drainage area in the
114 Himalaya (55,000 $km^2$), with two-thirds being located in China (Tibet) and one third in India
115 (Figure 1). Starting at the mountain front, surface elevations range from 400 m to 7200 m asl.
116 More than 80% of the catchment area is located in the semi-arid to arid orogenic interior at
117 elevations >4000 m asl, which results in a catchment-average elevation of 4400 m asl
118 (Supporting material - Figure S1). Vegetation cover is thick and dense at lower elevations at
119 the mountain front, but decreases rapidly above an elevation of 3000 m asl and is virtually
120 absent >3500 m asl. Therefore, the primary land cover in the Sutlej Valley is bare ground
121 (81.7 %), as compared to trees and shrubs (7.2 %), cultivated areas (6.8 %), glaciers (3.2 %),

and lakes (1.1 %) [*FAO*, 2009] (Table 1). Soil cover is present only in the lower part of the Sutlej catchment, which constitutes a small fraction (<15%) of the entire drainage area and therefore is likely to have a low impact on overall water storages.

Precipitation in the western Himalaya has pronounced seasonal and spatial variations [*Bookhagen and Burbank*, 2010]. Snowfall occurs mostly between December and March and increases with elevation and relief [*Immerzeel et al.*, 2012; *Singh and Kumar*, 1997; *Winiger et al.*, 2005]. During the summer months, the Indian monsoon (mid July – mid September) accounts for intense rainfall, which is mostly focused along orographic barriers of the southern Himalayan front and creates a steep SW-NE rainfall gradient, with >2 m/yr at the fontal parts to <0.2 m/yr over a horizontal distance of <100 km encompassing a mean elevation range of >4.000 m [*Bookhagen and Burbank*, 2006; *Wulf et al.*, 2010]. Although most monsoonal moisture is blocked by the High Himalaya, during active monsoon phases, strong convective cells sometimes migrate across this barrier and result in cloudbursts that can mobilize enormous amounts of sediments [*Bookhagen et al.*, 2005; *Craddock et al.*, 2007; *Hobley et al.*, 2012; *Wulf et al.*, 2010].

# 3 The hydrological model

## 3.1 Runoff production

The newly set up distributed hydrological model calculates runoff during each time step (1 day) at each cell in the gridded model space, i.e., digital elevation model (DEM), and routes the water through the river network taking flow times and runoff storage into account. Daily runoff production, $RP$ (mm/day), at a given location is the sum of snow melt ($M_s$), glacier melt ($M_g$), and rainfall ($P_r$), reduced by evapotranspiration ($ET$), according to:

$$RP = M_s + M_g + P_r - ET \quad (1)$$

The input data for rainfall and evapotranspiration are based on calibrated remote-sensing products, and discussed in section 4.2 and 4.3. In contrast, snow and glacier melt are computed by processing multiple remote-sensing datasets.

### 3.2 Snow- and glacier melt

Similar to previous studies [*Brubaker et al.*, 1996; *Hock*, 1999; 2003; *Martinec*, 1975; *Pellicciotti et al.*, 2005; *Rango and Martinec*, 1995], we use a temperature-index model that incorporates the influences of solar radiation, snow albedo, and cloud cover. Daily snow melt (mm/day) is calculated for every snow-covered cell according to:

$$M_S = \begin{cases} (T \cdot tf_s + R_{sw} \cdot srf_s) \cdot A_s, & T > T_t \\ 0, & T \leq T_t \end{cases} \quad (2)$$

where $T$ (°C) is the mean daily temperature, $R_{sw}$ (W/m$^2$) is the mean daily net shortwave radiation, $A_s$ (m$^2$) is the snow-covered area, $tf_s$ (mm °C$^{-1}$ day$^{-1}$) is an empirical *temperature factor* for snow melt, and $srf_s$ (mm W$^{-1}$ m$^2$ day$^{-1}$) is an empirical *shortwave radiation factor* for snow melt. $T_t$ is a threshold temperature above which melt is assumed to occur (e.g., 0°C). Glacier melt $M_g$ (mm/day) is calculated similarly but occurs only if the corresponding cell is ice-covered and snow-free:

$$M_G = \begin{cases} \left(T \cdot tf_g + R_{sw} \cdot srf_g\right) \cdot (A_{ice} + df \cdot A_{debris}), & T > T_t \\ 0, & T \leq T_t \end{cases} \quad (3)$$

where $A_{ice}$ (m$^2$) is the glacier area with clean ice exposure, $A_{debris}$ (m$^2$) is the glacier area with debris cover, $df$ is a dimensionless scaling factor for reduced melt rates on debris covered ice, and $tf_g$ (mm °C$^{-1}$ day$^{-1}$) and $srf_g$ (mm W$^{-1}$ m$^2$ day$^{-1}$) are empirical coefficients that relate temperature and shortwave radiation, respectively, to melt water production. Because supraglacial debris cover with a thickness >2 cm, reduces ice melt due to its shielding effect on radiation and heat fluxes [*Braun et al.*, 1993; *Huss et al.*, 2008; *Mattson et al.*, 1993; *Reid*

167 *and Brock*, 2010], we introduce a debris factor, *df*, that allows reducing melt rates for debris-
168 covered ice.

169 Net shortwave radiation, $R_{sw}$, is calculated as [*Pellicciotti et al.*, 2005]:

170 $$R_{SW} = R_{sky} \cdot f_{cc} \cdot (1 - \alpha) \quad (4)$$

171 where, $R_{sky}$ (W/m$^2$) is the incident clear sky solar radiation, $f_{cc}$ is a calibrated dimensionless
172 factor, ranging between 0.61 and 1 (see section 4.4.3), which accounts for reduction of clear
173 sky radiation due to cloud cover, and $\alpha$ is the snow or ice albedo.

174 **3.3 Runoff response**

175 This runoff response module is based on the HBV model concept [*Bergström*, 1976; 1992].
176 Similar to the hydrological modeling system PREVAH [*Gurtz et al.*, 1999; *Viviroli et al.*,
177 2009], we account for runoff storage in subsurface reservoirs by two linear storages (*SUZ* and
178 *SLZ*; Figure 2). We use these reservoirs to differentiate between surface runoff [*RS*
179 (mm/day)], interflow [*RI* (mm/day)], and groundwater runoff [*RG* (mm/day)] by modeling a
180 specific runoff response for each component (Figure 2). The groundwater storage is further
181 divided into fast (*RG1*) and slow-leaking (*RG2*) components. The sum of all runoff
182 components for each time step (*t*) corresponds to simulated river discharge ($Q_{sim}$):

183 $$Q_{sim}(t) = RS(t) + RI(t) + RG1(t) + RG2(t) \quad (5)$$

184 Water flows are computed for each time step (*dt*), which can be defined arbitrarily. We use
185 daily intervals based on the daily data availability of MODIS and TRMM remote sensing data
186 and river discharge measurements. Daily runoff production (*RP*) replenishes the upper storage
187 reservoir (*SUZ*) to generate interflow and additional surface runoff, if a certain storage
188 threshold is exceeded [$SI_{max}$ (mm)]. Water in the *SUZ* drains by percolation [*PERC*
189 (mm/day)] into the lower groundwater reservoir (*SLZ*), from where groundwater runoff

occurs. This hydrologic budget of both reservoirs is described by the following governing equations:

$$SUZ(t) = SUZ(t-1) + (RP(t) - (PERC(t-1) + RS(t-1) + RI(t-1))) \cdot dt \quad (6)$$

$$SLZ(t) = SLZ(t-1) + (PERC(t) - RG1(t-1) - RG2(t-1)) \cdot dt \quad (7)$$

The residence period of each runoff component (*RI, RS, RG1, RG2*) is controlled by the storage time parameters [*K0-K3* (day)]. Consequently, the generation of interflow (*RI*) and surface runoff (*RS*) depends on the content of the upper storage reservoir (*SUZ*) and the storage time parameters (*K1, K0*).

$$RI(t) = SUZ(t) \cdot \left(1 - e^{-\frac{t}{K1}}\right) \cdot dt^{-1} \quad \text{if } SUZ > 0 \quad (8)$$

$$RS(t) = (SUZ(t) - SI_{max}) \cdot \left(1 - e^{-\frac{t}{K0}}\right) \cdot dt^{-1} \quad \text{if } SUZ > SI_{max} \quad (9)$$

A threshold on the percolation rate [$PERC_{max}$ (mm/day)] limits the flux into the groundwater reservoir. Groundwater storage is divided into a fast-leaking storage (*SG1*) and a slow-leaking storage (*SG2*), which are filled by recharge rates [*GR1, GR2* (mm/day)] as a function of the percolation rate (PERC) [*Schwarze et al.*, 1999]. The fast groundwater component [*RG1* (mm/day)] is limited by a maximal storage capacity [$SG1_{max}$ (mm)], whereas the slow groundwater component [*RG2* (mm/day)] has no upper limit. The generation of groundwater runoff is governed by the storage time parameters (*K2, K3*) and the change in storage of the groundwater reservoirs during *dt*. Constant and tunable model parameters for each catchment are listed in Table 2.

$$RG1(t) = \left[SG1(t-1) \cdot \left(e^{-\frac{t}{K2}}\right) + \left(1 - e^{-\frac{t}{K2}}\right) \cdot GR1(t-1) \cdot K2\right] / K2 \quad \text{if } SLZ > 0 \quad (10)$$

$$RG2(t) = \left[SG2(t-1) \cdot \left(e^{-\frac{t}{K3}}\right) + \left(1 - e^{-\frac{t}{K3}}\right) \cdot GR2(t-1) \cdot K3\right] / K3 \quad \text{if} \quad SG1 > SG1_{max} \tag{11}$$

### 3.4 Runoff routing

To account for discharge travel times, we estimated flow velocities, *v* (m/s), based on a modified version of Manning's formula, according to:

$$v = sf^{-1} \cdot HR^{0.66} \cdot S^{0.5} \tag{12}$$

where, *S* (m/m) is the local channel gradient, *HR* (m) is the flow hydraulic radius and *sf* (dimensionless) represents a scaling factor, which is equivalent to Manning's roughness factor, to adjust the flow velocity to field observations from the Sutlej River [*Schulze et al.*, 2005] (Figure 3). For simplicity, we assume a rectangular Sutlej River cross section and calculate hydraulic radius as a function of the river depth (*D*) and river width (*W*):

$$HR = D \cdot W \cdot (2 \cdot D + W)^{-1} \tag{13}$$

We estimate river depths and widths based on a power-law scaling with bankful discharge, $Q_{bf}$ [e.g., *Allen et al.*, 1994; *Leopold and Maddock*, 1953]:

$$D = x_d \cdot Q_{bf}^{y_d} \tag{14}$$

$$W = x_w \cdot Q_{bf}^{y_w} \tag{15}$$

We use the coefficients from *Allen et al.* [1994] ($x_d$ = 2.71, $y_d$ = 0.557, $x_w$ = 0.349 and $y_w$ = 0.341), which are based on regression analysis with a dataset of 674 river cross sections across the USA and Canada. While measurements from satellite imagery to the east of our study area corroborates an exponent $y_w$ close to ~0.4 as a general average, there exists considerable channel-width variability between contrasting lithologic and tectonic regimes

232 that cannot currently be accounted for with a simple power-law approach [*Fisher et al.*,
233 2013].

234 For simplicity, we assume that hydraulic radii for non-bankfull discharge follow the same
235 geometric rule as for bankfull discharge. Hence Eqs. (14) and (15) are used to calculate the
236 hydraulic radius in Eq. (13) based on the mean annual discharge. We account for seasonally
237 varying flow times by scaling winter flow path times according to flow velocity
238 measurements (1.54 m/s in winter, 3.20 m/s in summer) of the Sutlej River at Luhri (31.34°N,
239 77.42°W) close to the mountain front at Bhakra [*Pandit et al.*, 2010] (Figure 3). Based on
240 these mean river discharge velocities, obtained by repeated float method measurements using
241 a surface velocity correction factor of 0.7, the scaling factor *sf* in Eq. (12) ranges between
242 0.549 (winter) and 0.264 (summer). These scaling factor values are relatively high in
243 comparison with other Manning's roughness factors, which can be attributed to the simplified
244 assumption of a rectangular riverbed with estimated river depths at bankful discharge. To
245 derive discharge lag times based on the average flow path velocity we calculated the
246 euclidean distance of each cell to the catchment outlet along the flow paths by the D8 flow
247 accumulation algorithm. Drainage networks and flow paths were extracted using the
248 TopoToolbox v2 [*Schwanghart and Scherler*, 2014]. Finally, we delayed runoff for each pixel
249 according to its average daily flow time from the pixel location to the drainage basin outlet
250 (Figure 3). This delay is measured in days ($t$) and sub-daily fractions (hourly delay) between
251 day ($t$) and day ($t$+1) based on the inverse ratio of the fractions.

252 # 4 Model input data and calibration procedures

253 ## 4.1 Ground station data

254 The available weather station data comprise 63 weather stations from the Indian
255 Meteorological Department (IMD), 17 high-elevation stations operated by the Bhakra Beas

256 Management Board (BBMB) and three weather stations that are part of the World
257 Meteorological Organization's (WMO) Regional Basic Climatological Network (Figure 1).
258 The IMD stations record rainfall only, whereas the BBMB and WMO stations additionally
259 measure snow water equivalent (SWE) by melting daily amounts of snow captured in a snow
260 gauge. Furthermore, all WMO and four BBMB stations (Figure 1) record daily maximum and
261 minimum temperatures, including one automated weather station at Khab that records hourly
262 data of rainfall, temperature, and incident solar radiation. We preprocessed the precipitation
263 data according to quality-control measures introduced by *Einfalt and Michaelides* [2008] and
264 excluded unreliable values from subsequent analyses [*Wulf et al.*, 2010]. In total, the available
265 precipitation records cover a fourteen-year time span from 1998 to 2012, but lack
266 completeness by 52% on average. The weather stations cover a steep north-south precipitation
267 gradient across the main Himalayan crest and range in elevation from 250 m to 4280 m asl
268 [*Wulf et al.*, 2010] (Supporting material - Table S1). We use these precipitation records to
269 calibrate and adjust the TRMM 3B42 rainfall data set.

270 In the Indian part of the Sutlej Valley, several privately owned and governmental hydropower
271 companies operate a dense network of river-gauging stations. Most station records cover the
272 time span from January 2004 to August 2008, although a severe flood in the Sutlej River on
273 June 26, 2005 has led to interruptions at five stations, lasting 1-8 months [*Wulf et al.*, 2012].
274 The daily discharge measurements are based on stage-discharge rating curves that are
275 annually recalculated during low-flow conditions in winter due to channel-bed changes. We
276 use river-discharge records from five gauging stations on the Sutlej River and four of its
277 major tributaries to calibrate and validate our model. This procedure enables us to quantify
278 the discharge components, their uncertainties, and their spatial variation across different
279 climatic zones in the Sutlej catchment.

## 4.2 Rainfall

To compute runoff due to rainfall, $P_r$, in our hydrological model, we tested three approaches that yield rainfall estimates with increasing spatial complexity. The first and simplest approach was to use the weather-station data and interpolate the rainfall records based on a 2D Delaunay triangulation-based interpolation method, which weights the area-of-influence associated to each weather station and performed well in previous studies with sparse data locations [*Preparata and Shamos*, 1985]. In our second approach we used a daily satellite-derived rainfall record, based on the TRMM product 3B42 (version 7), which has a spatial resolution of 0.25° x 0.25° (~30 km x 30 km) and a temporal resolution of 3 hours. This data set combines microwave and infrared rain-rate estimates from sensors onboard several low-earth orbit and one geosynchronous satellite, which are rescaled to monthly rain-gauge data [*Huffman et al.*, 2007]. Previous studies suggest that the TRMM 3B42 product is comparable to other satellite based rainfall products, which generally show a lower performance in complex terrain [e.g., *Dinku et al.*, 2008; *Maussion et al.*, 2011; *Sapiano*, 2009; *Tian et al.*, 2009]. Although the spatial resolution of the TRMM 3B42 data makes direct comparison to weather station data difficult, *Pan et al.* [2010] found in a comparison of different satellite-based precipitation products for the United States that rain-gauge assisted corrections of satellite products significantly enhance their skill in hydrologic predictions, especially over mountainous areas.

To assess the potential requirement for correcting the TRMM-based rainfall, we compared the TRMM 3B42 product with 84 weather station rainfall records across our study area. In general, TRMM captures rainfall at the humid range front with mismatches <6% during all months of the year, but overestimates rainfall by up to ~100% in the arid interior parts (Figures 4, 5). The mismatch in the arid areas is most pronounced during the summer season (May-October). During the winter season TRMM data also indicate substantial rainfall in the

high-elevation orogenic interior (Figure 4B), despite concurrent snow coverage and temperatures below freezing. Given the coinciding increase in TRMM rainfall rates with snowfall, it appears that the TRMM data has difficulties in these areas to distinguish between snow and rainfall.

Figure 5A shows the ratio between mean annual rainfall based on TRMM data and on weather station data for each of the weather stations, and thus by how much the TRMM data over- or under-predicts the ground measurements. Rainfall is overestimated in the arid interior part of the range by a factor of 2-5, whereas it is underestimated at the humid range front by up to 50% (Figure 5C). These data follow a negative power-law relation with a high coefficient of determination. It is currently not clear if this is a systematic bias in the TRMM-based rain rate, an effect of the temporally sparse sampling of the satellite product or due to the high spatial variability of rainfall and associated aliasing. To further test the ability of TRMM to detect individual rainfall events we compared daily rain rate observations by TRMM with the weather station records (Figure 5B). In this comparison we examine the TRMM performance based on its ability to detect (hit, *H*), not detect (miss, *M*), or erroneously predict (false alarm, *FA*) rainfall events. We only consider rainfall records above 2 mm, which represents the minimum recording level of weather stations. The false alarm rate (*FAR*) and hit rate (*HR*) are calculated according to *Jolliffe and Stephenson* [2003] and *Swets* [1986] by:

$$FAR = FA \cdot (H + FA)^{-1} \cdot 100 \quad (16)$$

$$HR = H \cdot (H + M)^{-1} \cdot 100 \quad (17)$$

Similar to the trend in mean annual rainfall we find a reasonably good performance (~70% hit rate, ~40% false alarm rate) of the TRMM data at the orogenic front, whereas towards the

328 interior of the orogen, TRMM has slightly fewer hits (~60%) and a much higher false alarm
329 rate (~70%).

330 In summary, our comparison revealed that the performance of the TRMM data increases with
331 increasing rainfall amounts throughout the region, but is relatively low where rainfall is low,
332 such as in the orogenic interior. To overcome this problem, we first filtered the satellite-based
333 rainfall data using MODIS snow cover data (see section 4.4.1) and air temperature data (see
334 section 4.4.2). TRMM rainfall events are filtered out in areas with daytime temperatures
335 below 0°C and are scaled in areas with snow cover by the inverse snow cover fraction.
336 Second, we scaled the daily TRMM observations with a spatially varying factor that is based
337 on the power-law scaling relation between mean annual rainfall derived from TRMM and the
338 ground stations (Figure 5A). With this third re-calibration approach, we aim to capture
339 adequately the reduction in rainfall towards the high-elevation arid orogenic interior and to
340 remove snow-rain confusionat higher elevations throughout the year. In the results section
341 5.1, we evaluate the model performance using three different rainfall datasets: (1) the
342 interpolated weather station data, (2) the original TRMM rainfall, and (3) the re-calibrated
343 TRMM rainfall data.

344 **4.3 Evapotranspiration**

345 Evapotranspiration in our model is based on the MODIS Global Terrestrial
346 Evapotranspiration Product (MOD16A2), which is available at
347 ftp://ftp.ntsg.umt.edu/pub/MODIS/Mirror/MOD16/MOD16A2.105_MERRAGMAO/ [*Mu et*
348 *al.*, 2011; *Mu et al.*, 2009]. The evapotranspiration algorithm is based on a physical model
349 using the Penman-Monteith method and considers surface-energy partitioning and
350 environmental constraints, such as vegetation cover and meteorological conditions, on
351 evapotranspiration [*Cleugh et al.*, 2007; *Monteith*, 1965; *Mu et al.*, 2007]. The current
352 algorithm also includes nighttime evapotranspiration and soil-heat flux among other

353 improvements and has been evaluated across different terrain and land cover types in North
354 America where it shows reasonable good correlation ($r^2 = 0.81$) with ground-based data [*Mu*
355 *et al.*, 2011].

356 The gridded evapotranspiration data are 8-day composites with a spatial resolution of 1 km.
357 After resampling the data to the spatial resolution of the model domain, we disaggregated the
358 8-day composite to daily data by linear interpolation between two 8-day composites. Because
359 there are no developed soils and associated vegetation covers in more than 85% surface area
360 of the Sutlej catchment, we assume near-surface soil water storage is negligible. Therefore we
361 consider only evaporation from the surface layer during days with rainfall. The resulting
362 effective precipitation (rainfall reduced by evapotranspiration) represents the daily budget of
363 rainfall and evapotranspiration within a modeling cell. If daily evapotranspiration exceeds
364 rainfall, the effective rainfall is set to zero. The effective precipitation has an average annual
365 evapotranspiration fraction of 0.21, which agrees reasonably well with field-based data from
366 the Central Himalaya, where ~15% of the daily moisture supply is recycled by
367 evapotranspiration [*Barros and Lang*, 2003].

368 **4.4 Snow and ice melt components**

369 **4.4.1 Fractional snow cover (FSC)**

370 Snow melt in our model occurs when a given pixel is snow covered and temperatures are
371 above zero. However, we excluded lake areas from our snowmelt module, because snowmelt
372 on frozen lakes does not infiltrate into the ground, as it gradually turns into lake water with a
373 considerable time delay. In our model we used daily fractional snow cover (FSC)
374 observations that are derived from the MODIS instrument onboard the Terra and Aqua
375 satellites of the NASA Earth Observation System. The globally available MOD10A1 (Terra)
376 and MYD10A1 (Aqua) products (current version 5) provide daily observations of FSC and
377 snow albedo, with a spatial resolution of 500 m [*Hall et al.*, 1995]. Terra images are available

since March 2000 and Aqua images since July 2002. The MODIS snow detection algorithm employs the normalized difference snow index (NDSI), which determines the difference in reflectance of snow between visible and short infrared wavelengths [*Hall et al.*, 1995; *Hall et al.*, 2002]. FSC gives the fraction of a pixel, which is snow covered, and is computed from a functional relationship between MODIS NDSI and higher resolution Landsat FSC data [*Salomonson and Apple*, 2004]. Comparison of MODIS snow products with ground measurements in the western US and Austria have yielded accuracies of 94% to 95% [*Klein and Barnett*, 2003; *Parajka and Blöschl*, 2006]. However, it should be noted that characterizing snow cover by spectral mixing is more accurate than empirical methods based on the NDSI, especially during periods of accumulation and melt [*Rittger et al.*, 2013].

The utility of the MODIS snow-cover products for hydrological modeling is limited by cloud cover, which causes data gaps. We reduced these data gaps by first complementing missing Terra data with Aqua snow-cover observations from the same day [*Dozier et al.*, 2008; *Gafurov and Bárdossy*, 2009]. As a result, the average data gaps in Terra FSC imagery reduce from 37.4±27.8% to 31.9±26.5%. In a next step, we corrected for artifacts introduced by large viewing angles and other systematic errors with spline interpolation on the FSC time series. The smoothing splines are weighted based on the sensor zenith angle, which is provided in the MODIS surface reflectance product MOD09GA [*Dozier et al.*, 2008]. Finally, we filled the remaining data gaps, with average durations of 2.1 days, by piecewise linear interpolation [*Fritsch and Carlson*, 1980].

Besides cloud-cover gaps, the daily MODIS snow-cover product is also affected by snow/cloud discrimination errors [*Dozier et al.*, 2008; *Hall and Riggs*, 2007]. Despite improvements in the cloud detection algorithm in the recent version (v5), the MODIS snow-cover algorithm occasionally confuses cloud with snow cover. These problems are associated with cloud-shadowed land and cloud type identification errors [*Hall and Riggs*, 2007]. It is

403 important to filter out these confusions, as they are typically associated with low elevations
404 and high temperatures, which can cause considerable snow-melt runoff. To filter erroneous
405 snow cover we calculated the daily average snowmelt elevation and excluded all snow cover
406 that is 2000 m below this reference.

407 Based on this snowmelt elevation filter, we analyze the temporal distribution of clouds
408 misclassified as snow for the combined Aqua and Terra FSC observations (Figure 6). Here,
409 we find pronounced snow/cloud confusions during the monsoon season, when the Himalayan
410 front is affected by a dense monsoonal could cover and annual snow cover is at its minimum.
411 Because these snow misclassifications are often associated with high summer temperatures,
412 they increase annual snowmelt in Sutlej Valley by about 1.8%.

413 **4.4.2 Temperature**

414 We tested three different strategies to compute air temperatures and evaluated the accuracy of
415 each approach by comparing generated temperatures with weather station records to use the
416 most favorable approach in our hydrological model. The simplest chosen approach is based
417 on the extrapolation of weather station air temperatures from Kalpa (Figure 1) using a
418 constant atmospheric lapse rate of -6.5°C/km [*Barry and Chorley*, 2003]. The second
419 approach incorporates temperature data from five weather stations to calculate a seasonally
420 varying atmospheric lapse rate. We use daily minimum and maximum temperatures from
421 weather stations in Patiala (250 m), Dehradun (680 m), Kalpa (2730 m), Rakchham (3130 m),
422 and Namgia (2840 m) to calculate the daily day and nighttime air temperature lapse rate (cf.
423 Figure 1). Depending on seasonal variations in the atmospheric moisture content we observe a
424 high lapse rate during winter and a low lapse rate during summer (Figure S2) [*Dury*, 1981].
425 Accentuating the seasonal lapse-rate trend we calculate a mean daily lapse rate for the day
426 and nighttime, which we use to extrapolate minimum and maximum air temperatures

427 measured in Kalpa. The mean annual lapse rate is -5.2±1.6°C/km and -5.7±1.0°C/km for day-
428 and nighttime, respectively.

429 The third approach is based on the MODIS land surface temperature (LST) product
430 (MOD11A1 and MYD11A1) [*Wan et al.*, 2004], which we calibrated with local weather
431 station data to derive a distributed daily air temperature dataset. The MODIS-derived LST
432 data are based on the view-angle dependent split-window LST algorithm, which corrects for
433 atmospheric and emissivity effects in the thermal infrared signal over various land cover types
434 [*Wan and Dozier*, 1996]. Refinements in the algorithm of the latest LST version 5 improved
435 the accuracy and stability of LST data especially in high-altitude regions [*Wan*, 2008]. Most
436 validation studies indicate that the accuracy of MODIS LST data is better than 1 K [*Coll et*
437 *al.*, 2005; *Wan*, 2008; *Wan et al.*, 2004]. However, the precise retrieval of snow-surface
438 temperatures is difficult, because snow emissivity varies with the sensor viewing angle
439 [*Dozier and Warren*, 1982]. In addition, mixed pixels, which show exposed land and snow
440 cover within the 1x1 km MODIS LST area, are likely to further complicate the snow
441 temperature retrieval.

442 Temperature-index models for estimating snow and ice melting are usually run with above-
443 ground air temperatures, which reflect both, incoming longwave atmospheric radiation and
444 sensible heat flux, and thereby more than three-quarters of the entire energy source for
445 melting [*Ohmura*, 2001]. The difference between surface and air temperatures is mainly
446 controlled by the surface energy balance [*Prince et al.*, 1998]. Therefore, shortwave radiation
447 fluxes (e.g., solar radiation), strongly affect daytime surface temperatures, whereas their
448 impact on nighttime temperatures is minor. The correlation of MODIS day- and nighttime
449 LST with daily maximum and minimum air temperatures of five weather stations in our study
450 area illustrates these differences (Figure 7). Based on these relations, we calculated the
451 corresponding air temperature of Aqua and Terra LST observation.

Similar to the snow cover data, the LST data are affected by data gaps due to cloud cover and by other distortions due to steep sensor viewing angles. We reduced these data gaps at first by combining successive Terra and Aqua observations from the same day and the same night. As a result, the average data gaps during the daytime (Terra: 39.7±27.6% (mean±1 sigma standard deviation); Aqua 47.3±26.9%) and nighttime (Terra: 30.3±23.1%; Aqua 28.9±21.9%) observations reduce to 33.6±26.9% and 21.7±21.4%, respectively. In a next step, we replaced missing data based on linear regressions between scaled MODIS temperature time series of each pixel and the air temperature record of the weather station in Kalpa (see Figure 1), weighted by the sensor viewing angles. In addition, we used the associated *quality check* datasets (QC_day and QC_night) of the MOD11A1 product to reduce regression weights by half for MODIS LST data flagged with "other quality". Finally, we corrected for artifacts in the scaled MODIS temperatures introduced by large viewing angles and other systematic errors with weighted spline interpolation in analogy to the final snow cover processing procedure.

The correlation of air temperatures derived by our three approaches with air temperature records from weather stations at Rakchham, Namgia, Patiala, and Dehradun (cf. Figure 1) shows that scaled MODIS day and nighttime temperatures yield the best results (Table 3, Figure S4). Therefore, we use our third approach based on MODIS data to calculate air temperatures that drive snow and glacier melt.

#### 4.4.3 Incoming shortwave radiation

The incoming shortwave radiation (clear sky radiation) is calculated using standard GIS procedures that account for direct and diffusive components [*Böhner and Antonic*, 2009]. All parameters of the radiation module are given in Table S2. We computed daily averages of quarter-hourly free sky incoming solar radiation for each specific model cell location, based on a digital elevation model derived from the Shuttle Radar Topography Mission (version 2)

477 [*Farr et al.*, 2007], where voids have been patched with data from topographic maps (J. de
478 Ferranti, 3″ resolution digital elevation data for Asia, 2007,
479 http://www.viewfinderpanoramas.org/dem3.html).

480 Clouds reflect and absorb incoming solar radiation [*Stephens et al.*, 1996] and therefore
481 reduce snow and glacier melt [*Pellicciotti et al.*, 2011]. We estimate this reduction in our
482 study area by comparing observed solar radiation, measured at Khab (Figure 1), with the
483 computed clear sky radiation and the daily cloud cover (Figure 8).

484 We derived a daily fractional cloud cover (FCC) for each pixel by averaging the cloud-flags
485 (0 for cloud-free and 1 for cloud-covered) from the FSC products by the Aqua and Terra
486 satellites. These two daily MODIS observations are acquired during late morning (mean solar
487 time: 10:51 ± 0:31 h) by Terra and early afternoon (mean solar time: 13:13 ± 0:30 h) by
488 Aqua. We used the relation stated in Figure 8C to account for reduction in incoming solar
489 radiation due to cloud cover and calculated the mean daily net shortwave radiation according
490 to Eq. 4 (see section 3.1). The snow albedo used in Eq. 4 is part of the MODIS snow-cover
491 product, which we processed by the same methodology as described for the snow cover
492 product (see section 4.4.1). For glacial surface areas we used a constant surface albedo of 0.34
493 for debris-free ice and 0.15 for debris-covered ice [*Brock et al.*, 2010].

494 **4.4.4 Glacial cover**

495 We used the Randolph Glacier Inventory provided by the Global Land Ice Measurements
496 from Space Initiative (GLIMS) available at http://www.glims.org/RGI/, which was recently
497 updated based on the study by *Frey et al.* [2012] to provide a comprehensive glacier inventory
498 of the western Himalaya (GLIMS, and NSIDC, 2012). The data provided by *Frey et al.*,
499 [2012] are based on classification of Landsat ETM+ Band 3 / 5 ratio images from September
500 2001 and Palsar coherence images to distinguish between debris-free and debris-covered
501 glacial parts. We neglect changes in glacial coverage during our study period, because these

are small compared to the 500-m spatial resolution of our model [*Scherler et al.*, 2011]. Based on the high-spatial resolution (30 m) of the ice-cover data we generated fractional debris-free and debris-covered ice areas for each model cell that contains ice (Figure 9). The total glaciated area within the Sutlej catchment accumulates to 1761 $km^2$ that corresponds to 3.2% of which ~8% are debris-covered.

### 4.5 Model application and calibration

Based on our enhanced distributed hydrological model and the remotely sensed input data we simulated river discharge at nine locations (stars in Figure 1) covering various spatial scales and climatic environments (Table 1). We calculate daily runoff from April 2000 to December 2012 at each cell in the gridded model space (463 m) of the Universal Transverse Mercator (UTM) projection 44N.

Previously, we introduced a set of tunable and constant parameters, which drive the hydrological model (Table 4). To calibrate the snow- and glacier melt, we use four adjustable parameters ($srf_S$, $tf_S$, $srf_G$, $tf_G$). In our runoff response approach, we use the minimum of three more adjustable parameters ($SI_{MAX}$, $SG1_{MAX}$, $PERC_{MAX}$) to avoid complex parameter interaction (Table 4). Furthermore, the runoff response module includes four constants (*K0, K1, K2, K3*), which were adopted from default values of the PREVAH hydromodel [*Viviroli et al.*, 2007]. Additional constant parameters of the snow and melt module include the threshold temperature ($T_t$) of 0°C and the debris factor (*df*) of 0.7 to account for reductions in glacier melt due to thick debris cover. This debris factor is derived from annual surface mass-balance measurements (2002-2010) of debris-covered and debris-free parts on the Chhota Shigri glacier in the neighboring Chandra river basin [*Azam et al.*, 2012], which we consider to be representative for a generally thick and widespread debris cover in the western Himalaya [*Scherler et al.*, 2011].

We define the range of parameter values in the snow- and glacier melt module based on their contribution to river discharge. The lower and upper bound of each glacier melt factor can contribute 0% to 50% to observed river discharge, respectively. Likewise, the lower and upper bound of each snow-melt factor can contribute 0% to 90% to observed river discharge, respectively.

To calibrate the tunable parameters ($tf_S$, $tf_G$, $srf_S$, $srf_G$, $SI_{max}$, $SG1_{max}$, $PREC_{max}$), we used an automatic optimization method that finds the best model performance based on the Nash-Sutcliffe efficiency (*NSE*) [*Nash and Sutcliffe*, 1970] and the relative volume error (*RVE*) between simulated ($Q_{sim}$) and observed discharges ($Q_{obs}$) [*Akhtar et al.*, 2008]:

$$NSE = 1 - \frac{\sum_{i=1}^{N}[Q_{sim}(i) - Q_{obs}(i)]^2}{\sum_{i=1}^{N}[Q_{obs}(i) - \bar{Q}_{obs}]^2} \quad (18)$$

$$RVE = 100 \cdot \frac{\sum_{i=1}^{N}[Q_{sim}(i) - Q_{obs}(i)]}{\sum_{i=1}^{N} Q_{obs}(i)} \quad (19)$$

where $i$ is the time step, $N$ is the total number of time steps, $\bar{Q}_{obs}$ is the mean of $Q_{obs}$ over the calibration/validation period. For a favorable model performance ($p$), the NSE should be close to the maximum value of 1 and the RVE value should be close to zero.

$$p = \frac{NSE}{1 + |RVE|/100} \quad (20)$$

This constrained nonlinear optimization method finds the minimum (best performance) of a scalar function with several variables for a given initial estimate. By generating 100 random starting points for each of our seven tunable variables within their lower and upper limits we exclude local minima to confidently detect the best performance parameters for the global function minimum.

For each gauging station we divided the river discharge dataset in two halves, using the first data period to calibrate the model and the second period to validate its performance (Figure

548 10). The calibrated and constant model parameters that drive the snow- and glacier melt-
549 module and the runoff response module are given in Table 2.

550 We tested the model sensitivity to variations (10% incremental steps) of each calibration
551 factor for snow and glacier melt around their optimal values on model performance (Figure
552 11). The model sensitivity of single melt factors depends on the contribution of the respective
553 melt component to total river discharge, which varies among the river catchments. In general,
554 the hydrological model is more sensitive to variations in snow-melt factors as compared to
555 glacier-melt factors. Therefore, we conclude that variations in the reduction of glacier melt
556 below debris cover (factor 0.7 in this model) will have a low impact on the model
557 performance.

558 # 5 Results

559 ## 5.1 Simulated river discharge

560 First, we evaluate the model performance of the different rainfall datasets that are based on
561 (1) weather station data, (2) original TRMM 3B42 data, and (3) re-calibrated TRMM data
562 (see section 4.2). Both, the original TRMM 3B42 data and the interpolated weather station
563 dataset result in excessive rainfall runoff, which exceeds observed river discharge by more
564 than two orders of magnitude (Table 2) in the high-elevation arid regions of the southern
565 Tibetan Plateau (i.e., Spiti and Sutlej at Namgia catchments, cf. Figure 1). Excess rainfall in
566 the interpolated weather station dataset is due to the lack of weather station data in the high-
567 elevation arid regions. Therefore, rainfall events recorded at distant weather stations in semi-
568 arid regions are wrongly extrapolated to high-elevation arid regions. Similarly, missing
569 weather station data from the orogenic interior may affect the original TRMM 3B42 dataset,
570 as rainfall magnitudes cannot be rescaled to monthly rain-gauge data. Accordingly, the
571 original TRMM 3B42 data does not adequately represent the decrease in rainfall across the

572 Himalaya. We observe the best model performance using the re-calibrated TRMM rainfall
573 dataset, which also results in a realistic partitioning of discharge sources (Table 5).

574 Using the re-calibrated TRMM data, simulated river discharges capture very well the
575 observed discharges (Figure 12). However, high-elevation catchments with relatively large
576 rainfall contributions, such as Ganvi and the Sutlej catchment upstream of Namgia, are not
577 adequately represented as snowfall-dominated catchments. Apart from these two catchments,
578 the remaining watersheds yield high performance measures with NSE values ranking between
579 0.68 and 0.78 and show a high degree of consistency among each other (Table 5).

580 Our modeling results covering the period April 2000 to December 2012 indicate that annual
581 average Sutlej River discharge (Sutlej at Bhakra) is sourced approximately half by effective
582 rainfall (55±5.1%) and half by snow (35±5.1%) and glacier melt (10±3.4%) (Table 5). Along
583 its course from high to low elevations the contribution of glacier melt to Sutlej River
584 discharge decreases from about 30% to 10%. Rainfall dominates river discharge in
585 catchments at the Himalayan front, whereas snow melt dominates river discharge in the high
586 elevation southern Tibetan Plateau and the main Himalayan crest.

587 **5.2 Spatiotemporal distribution of hydrologic components**

588 In general, mean annual runoff within the Sutlej Basin is characterized by major regional
589 differences (Figure 13A). The southern Tibetan Plateau is characterized by low precipitation
590 and runoff due to its low relief and its location leeward of the main orographic barrier. The
591 high-relief region of the main Himalayan crest captures most winter snowfall, which is also
592 reflected by large numbers of glaciers (Figure 9). The resulting increases in snow and glacier
593 melt come along with moderate increases in monsoonal rainfall causing total river discharge
594 to rise by up to one order of magnitude. This region of pronounced snow and glacier melt
595 coincides with the steepest section of the Sutlej River profile where topographic relief is
596 highest (Figure 13A, 14B). In contrast, the Himalayan front is dominated by rainfall due to

lower surface elevations and its windward location along the main orographic barrier. Increasing vegetation cover and temperatures cause high evapotranspiration rates (ca. 0.4 m/yr) while snow and glacier melt decrease from ca. 60% to 0% in this area.

The cumulative runoff of each Sutlej River tributary (>100 $km^2$) shows that the Spiti and Baspa River are the major contributors of the Sutlej River (Figure 13B). Analysis of the relative contributions to Sutlej River discharge in the downstream direction reveals that snowmelt is the dominant runoff source in most of the high-altitude part of the catchment and down to a river elevation of ~590 m. Downstream of this point, which corresponds to a linear distance of about 40 km from the mountain front, effective rainfall becomes the dominant discharge component (Figure 13C).

We estimated the spatial distribution of snow melt for the period October 1$^{st}$, 2001 to September 30$^{th}$, 2012 by the "inverse melt" approach [*Molotch and Norte*, 2009] (Figure 14A). This annual summation of daily snow melt represents all the snow that melted during the hydrological year (October-September). Although snow can persist throughout the melt season at high elevations, snow accumulation areas are mainly restricted to glacial accumulation zones. Therefore, we assume that our snow-melt summation is roughly equal to annual amounts of snow water equivalent.

The snow-melt distribution varies across the western Himalaya with snow melt starting at surface elevations of about 1800 m asl that increases northeastward along with increases in elevation and relief (Figure 14B). Snow melt is high (>0.5 m) in the region of the main Himalayan crest, from where it decreases towards the Tibetan Plateau. Despite high elevations, this decline is mainly due to an increasing leeward distance from the main orographic barrier and a decrease in topographic relief that effectively captures orographic precipitation (Figure 14B). Accordingly, we find large spatial variations in glacier melt between glaciers situated in the Himalayan crest region and glaciers bordering the Tibetan

622 Plateau (Figure S5). Whereas low average ablation rates are typical for large ice fields in the
623 Himalayan crest region, generally high ablation rates characterize multiple small glaciers at
624 the southern Tibetan Plateau.

625 Annual river discharge throughout the Sutlej Valley is characterized by a pronounced
626 seasonal cycle with low flow during winter and peak runoff during summer (Figure 15). Snow
627 melt initiates in March and dominates river discharge until June regardless of geographic
628 location. During that period snow melt in the Sutlej Valley successively progresses to higher
629 elevations, with peak snow melt at elevations of 4500 to 5500 m asl. From June to September
630 monsoonal rainfall and glacier melt contribute approximately equal to river discharge at and
631 upstream of the main Himalayan crest.

632 **5.3 Annual variations of hydrological components**

633 The observed Sutlej River discharge at the mountain front has a high annual variability, with
634 discharge varying by almost a factor of two between individual years (i.e., 2004 and
635 2005/2010, Figure 16D). Comparing the annual variation of ground-based measurements with
636 simulated runoff of each hydrological component, we find that variations in snow melt ($r^2$ =
637 0.69) and re-calibrated TRMM-derived rainfall ($r^2$ = 0.64) are captured well (Figure 16A and
638 16B). We also find an inverse correlation ($r^2$ = 0.59) between the observed winter snowfall,
639 which is represented by snow melt (Figure 16B), and the glacier melt during the subsequent
640 summer (Figure 16C). In other words, when winter snowfall is high, glacier melting during
641 the following summer is low. The varying time spans of annual snow cover on glaciers and
642 thus the variation in the glacier melt duration explains 86% of the annual variations in glacier
643 melt. Thus, winter snowfall on glaciers contributes not only to glacial accumulation but also
644 influences glacial ablation, as prolonged snow cover shields glaciers from radiative heating in
645 the subsequent summer season [*Thayyen et al.*, 2007]. The modeled annual variations in
646 glacial ablation agree with ablation stake measurements of the nearby Chhota Shigri Glacier,

647 which reveal significant decreases in glacier melt during 2005, 2009, and 2010 [*Azam et al.*,
648 2012]. Our modeled mean specific ablation rates for the entire Sutlej catchment based on the
649 glacier melt contribution to river discharge and the glacial surface area (1761 $km^2$) vary
650 considerably between 2000 and 2012 with mean summer mass balance of -1.33±0.35 m/yr.

651 Differences in temperature and precipitation in the western Himalaya were particularly high
652 between 2004 and 2005. Low snow- and rainfall occurred in conjunction with high
653 temperatures in 2004, whereas high snow- and rainfall accompanied low temperatures in 2005
654 (Figure 17). As a result river discharge in 2004 was almost half the volume as of 2005.
655 However, the low runoff from snow melt and rainfall in 2004 was extenuated by high glacier
656 melt rates (17.3%), favored by high temperatures and a longer melting period due to low
657 snow cover on glaciers (Figure 17).

658 # 6 Discussion

659 ## 6.1 Limits of the hydrological model

660 Due to the remoteness and climatic variability of the Sutlej Valley it is difficult to model its
661 hydrology based on sparse ground-station coverage alone. Therefore, we based our
662 hydrological model on calibrated remote-sensing data, which we validated with a unique
663 ground-station dataset. Despite our use of remote-sensing data with high spatial and temporal
664 resolution, several shortcomings of the input data and the model setup warrant attention when
665 interpreting the results:

666 First, our modeling approach is deliberately simple to rule out unknown parameters that are
667 difficult to constrain. We neglected refreezing of snow and ice melt, sublimation of snow and
668 ice, losses to the groundwater system by deep seepage, turbulent energy exchange (e.g., rain
669 on snow events), and transient water storage in soils and vegetation. The latter may be of

lower importance in the upstream parts of our study area, because vegetation cover is only pertinent in the lower-elevation regions of the catchment area (Figure S1). However, larger discrepancies between observed and modeled river discharge at the lowermost gauging station at Bhakra (Figure 16D) potentially derive from lacking soil-water storage, especially during exceptionally warm and dry years with high soil infiltration rates as occurred in 2004. The effect of neglecting the aforementioned processes is difficult to estimate as relevant data on their implications on river discharge in the Himalaya is largely missing.

Second, there exists a trade-off in the TRMM 3B42 precipitation product between high temporal (3 h) but low spatial resolution (30 x 30 $km^2$). Consequently, TRMM 3B42 would not capture high-spatial variability of monsoonal rainfall that could result from small-scale convection, for example. However, the high sampling rate is crucial to detect the occurrence of convective monsoonal rainstorms that have short lifetimes of half an hour to several hours and small spatial footprints of a few to several dozen $km^2$ [*Barros et al.*, 2006]. Overall, we find that in those areas where annual rainfall is generally high (>0.7 m/yr), TRMM 3B42 performs reasonably well compared to the ground based measurements, whereas it performs poor in areas where annual rainfall is lower (<=0.7 m/yr). However, because the contribution of rainfall as compared to snow and ice melt to river discharge is much lower in the latter areas, we still obtain reasonable model results.

Third, the air temperature data that drive the thermal snow and glacier melt module are based on MODIS LST data, which we scaled by linear regressions with air temperature records from five weather stations. Despite the large altitudinal range of 2880 m among these stations, the relationship between air and surface temperatures may vary at higher elevations and in regions with contrasting land cover and radiation fluxes. This complexity may affect high-elevation low-relief region that experience high radiative heating during summer, but it presumably has a low impact on snow-covered areas and therefore snow melt.

Fourth, our shortwave-radiation and temperature factors for snow and ice melt (equations 2 and 3) are temporally constant but vary systematically between catchments as they decrease with increasing mean catchment elevation. These variations result from our model optimization process and might be related to the following causes: (1) Sublimation of snow and ice increases with elevation, which reduces the energy available for melt and thus lowers the corresponding melt factors [*Lang and Braun*, 1990]; (2) losses to the groundwater system by deep seepage are likely to increase with increasing catchment areas at higher elevations; and (3) larger discrepancies between actual and modeled temperatures at higher elevations may similarly affect melt factors to compensate for increased melt rates.

### 6.2 Benefits and limits of remote sensing data in hydrological models

Based on our modeling results and previous studies on remote sensing products we aim to evaluate the benefits and limits of remote sensing data in hydrological modeling studies. In this study we used different remote sensing products that are based on different wavelengths of the electromagnetic spectrum ranging from (1) reflected solar radiation for snow, cloud, and glacial cover as well as evapotranspiration via (2) thermal infrared emissions for land surface temperature data to (3) reflected microwave radiation data for rainfall rate estimates. Remote sensing observations bear the potential to detect the spatial and temporal variability of hydrometeorological states (e.g. snow cover) and fluxes (e.g. rainfall rate) with an associated uncertainty [*Schmugge et al.*, 2002]. These ambiguities derive from varying surface and atmospheric conditions, as well as specific sensor characteristics and data processing methods [*Dozier et al.*, 2008]. Consequently, remote sensing data need to be evaluated based on ground observations to verify their specific and general applicability in hydrologic models.

In general, satellite data can be highly beneficial in mountainous or remote regions with sparse ground observations and/or a high spatial variability in the state or flux of interest. In

720 most instances the value of remote sensing data for hydrological models depends on its ability
721 to detect the spatial and temporal variability of hydrometeorological states and fluxes. For
722 example, glacier outlines are characterized by relatively low temporal variations and can be
723 mapped accurately with sensors of high spatial resolution (e.g. Landsat) if challenges like
724 debris, snow, and cloud cover can be addressed [*Frey et al.*, 2012]. Similarly, moderate snow
725 cover and albedo changes in space and time can be depicted accurately with sensors of high
726 temporal resolution (e.g. MODIS, AVHRR) [*Hüsler et al.*, 2012; *Parajka and Blöschl*, 2006].
727 In contrast, convective monsoonal rainstorms have a relatively short lifetime, which makes it
728 challenging to detect their magnitude and spatial distribution with repetitive snapshots from
729 space (e.g. TRMM) [*Tian et al.*, 2009]. Therefore, ground-based rainfall records are highly
730 advantageous to calibrate remote sensing data on regional scales [*Huffman et al.*, 2007].
731 Overall, satellite-based precipitation products can significantly improve hydrologic
732 investigations in areas with sparse weather station records [*Pan et al.*, 2010]. Conversely, a
733 dense network of rainfall records is likely to outperform satellite-based rainfall estimates, as
734 indicated by the model performance comparison in the Baspa catchment (Table 5). Similarly,
735 we estimated cloud-cover fraction based on two measurements per day (i.e. MODIS Aqua and
736 Terra), which can be improved by including additional cloud-cover observations during the
737 daytime. Another challenge for snow and glacier melt models is to accurately infer air
738 temperatures in complex terrain [*Minder et al.*, 2010]. We compared three approaches to
739 compute air temperatures, which comprise: (1) seasonally constant lapse rate, (2) seasonally
740 varying lapse rate, and (3) MODIS LST scaling. Among these different air temperature
741 interpolation methods, we find the highest accuracies for the second and third approach.
742 Presumably, a remote sensing based approach to infer air temperatures outperforms a varying
743 lapse rate approach on regional scales (>10,000 $km^2$) with few weather stations, whereas the
744 latter approach is likely to be more suitable on smaller scales (<1000 $km^2$) with multiple
745 station records. In summary, it depends on the specific data availability if ground based,

746 spaceborne, or combined observations are most suitable to map out the spatial and temporal
747 variability of the state or flux of interest.

748 **6.3 Comparison with previous studies**

749 Previously, *Bookhagen and Burbank* [2010] and *Singh and Jain* [2003] modeled the
750 hydrological budget of the Sutlej River using different approaches. *Bookhagen and Burbank*
751 [2010] modeled mean monthly river discharge, based on TRMM 2B31 data to derive rainfall
752 quantities and MODIS data to model snowmelt and evapotranspiration. Their study indicates
753 a snowmelt and rainfall contributions of 57% and 43%, respectively [*Bookhagen and*
754 *Burbank*, 2010]. *Singh and Jain* [2003] modeled daily Sutlej River discharge for six years
755 between 1988 and 1999 based on isothets from ten rainfall stations to estimate rainfall
756 quantities and snow cover data derived from Landsat MSS and IRS LISS-I data to model
757 snow melt in different elevation zones. Their estimate of 68% snowmelt and 32% rainfall
758 contributions to the Sutlej River discharge, on average, is constrained to the Indian part of the
759 Sutlej River basin [*Singh and Jain*, 2003]. Considering the different modeling approaches,
760 model input data, spatial and temporal scales, and target areas it is not surprising that our
761 results (55% effective rainfall, 35% snow melt, 10% glacier melt) deviate from the latter
762 study.

763 Our estimate of average glacial ablation in the Sutlej catchment (1.33±0.35 m/yr) and average
764 range of snow accumulation (0-1.4 m/yr water equivalent) are well within range of glacier
765 mass balances estimates of -0.15 to -0.75 m/yr in the region [*Azam et al.*, 2012; *Berthier et*
766 *al.*, 2007; *Kääb et al.*, 2012; *Wagnon et al.*, 2007]. *Immerzeel et al.* [2012] estimated similar
767 precipitation magnitudes (1-2 m/yr) in regions >4000 m asl in the Hunza catchment of the
768 Karakorum based on glacier mass balance models. Moreover, we re-calibrated TRMM 3B42
769 rainfall estimates with measurement from more than 80 weather station, which further

770 compare well with river discharge magnitudes (Table 5). In addition, our melt parameters are
771 in general agreement with parameters used by *Pellicciotti et al.* [2005], although a direct
772 comparison of model parameters is generally hampered by a deviating modeling approaches
773 and varying geographic or climatic influences.

774 # 7 Conclusion

775 In this study, we provide a comprehensive analysis of hydrologic components and their
776 contribution to daily Sutlej River discharge, based on a simple hydrological model that uses
777 calibrated remote-sensing data. Model performance was improved by (1) filling cloud cover
778 gaps in the fractional snow cover data, as well as identifying cloud pixels misclassified as
779 snow, and correcting for viewing angle artifacts, (2) scaling MODIS surface temperatures to
780 observed air temperatures, (3) incorporating daily fractional cloud cover data in the net
781 radiation balance, and by (4) calibrating rainfall estimates based on TRMM 3B42 data with
782 data from 84 weather stations. Calibrating the rainfall data is particularly relevant in the Sutlej
783 catchment as the TRMM 3B42 data moderately well depicts rainfall in humid frontal regions
784 of the Himalaya within 6% mismatch of the mean monthly weather station records, but
785 significantly overestimates weather station rainfall by a factor of 2-5 in the orogenic interior
786 (elevations > 2000 m asl). This bias follows an inverse power-law relationship with mean
787 annual precipitation and suggests that TRMM 3B42 performs poorly in semi-arid to arid
788 regions of high relief and elevation.

789 Based on our modeling results, the average annual Sutlej River discharge at the mountain
790 front (Sutlej River at Bhakra) is sourced to ~55% by effective rainfall, ~35% by snow melt,
791 and ~10% by glacier melt. The discharge components vary strongly by season with snow melt
792 dominating (63%) the pre-monsoon season (April to June) whereas the summer season from
793 July to September is dominated by rainfall (61%), followed by snow (24%) and glacier melt

794 (15%). Thus, transient water storage in ice and snow is an important source for discharge in
795 the Sutlej River. Peak discharges and daily variations are usually controlled by rainfall events,
796 which increases the importance of transiently stored water sources to continuous downstream
797 water supply. This water storage is key for maintaining hydropower and agriculture in the
798 downstream areas of the Sutlej River.

799 Snow and glacier melt contributions to discharge in the western Himalaya is highest near the
800 main Himalayan crest, about 100 km inwards from the mountain front (Figure 14).
801 Downstream or windward of the main Himalayan crest, rainfall contribution becomes more
802 important during both the winter and summer seasons. Pronounced inter-annual variations in
803 winter snowfall also affect glacier melt, as the snow-cover duration controls radiation influx
804 during the subsequent summer season. Based on our model, the average glacier melt in the
805 Sutlej Valley between 2001 and 2012 has a water equivalent of 1.33±0.35 m/yr, averaged
806 over an ice-covered area of 1761 $km^2$. The importance of glacier melt to balance river
807 discharge variability and to countervail low precipitation runoff was particularly noticeable
808 during the exceptionally warm and dry year 2004. Under scenarios of future climate change,
809 including higher temperatures, rising snowlines and declining glaciers, the decadal-time scale
810 discharge of the Sutlej River is likely to become more variable and reduced, especially in the
811 high-elevation internal parts of the orogen.

812 ## Acknowledgements

813 This research was funded by the German Science Foundation (DFG, GRK 1364) and carried
814 out at Potsdam University and the GFZ German Research Centre for Geosciences. The data
815 used in this study were acquired as part of the Tropical Rainfall Measuring Mission (TRMM)
816 sponsored by the Japan National Space Development Agency (NASDA) and the NASA.
817 Bodo Bookhagen was supported with grants from NASA (NNX08AG05G) and NSF (EAR

0819874). We thank the employees of BBMB, HPSEB and JayPee Group, who generously shared their weather station and river discharge records with us. We also appreciate that Holger Frey provided his data on glacier outlines for us. We are grateful to Tashi Longpo, Swami Ray, and Bishan Lal for their enduring support during fieldwork. Ground station data used in this study (e.g. river discharge, precipitation) can be provided upon request to the corresponding author.

824 ## References


825 Akhtar, M., N. Ahmad, and M. J. Booij (2008), The impact of climate change on the water
826 resources of Hindukush-Karakorum-Himalaya region under different glacier coverage
827 scenarios, *Journal of Hydrology*, *355*(1-4), 148-163. doi:10.1016/j.jhydrol.2008.03.015.

828 Alford, D., and R. Armstrong (2010), The role of glaciers in stream flow from the Nepal
829 Himalaya, *The Cryosphere*, *4*(2), 469-494. doi:10.5194/tcd-4-469-2010.

830 Allen, P. M., J. C. Arnold, and B. W. Byars (1994), Downstream channel geometry for use in
831 planning level models, *Journal of the American Water Resources Association*, *30*(4), 663-
832 671. doi:10.1111/j.1752-1688.1994.tb03321.x.

833 Anderson, E. A. (1976), A point energy and mass balance model for a snow cover, 150 pp,
834 NOAA Tech Rep. 19, 150 pp, NOAA.

835 Azam, M. F., et al. (2012), From balance to imbalance: a shift in the dynamic behaviour of
836 Chhota Shigri glacier, western Himalaya, India, *Journal of Glaciology*, *58*(208), 315-324.
837 doi:10.3189/2012JoG11J123.

838 Bales, R. C., N. P. Molotch, T. H. Painter, M. D. Dettinger, R. Rice, and J. Dozier (2006),
839 Mountain hydrology of the western United States, *Water Resources Research*, *42*(8), 1-13.
840 doi:10.1029/2005WR004387.

841 Barnett, T. P., J. C. Adam, and D. P. Lettenmaier (2005), Potential impacts of a warming
842 climate on water availability in snow-dominated regions, *Nature*, *438*(7066), 303-309.
843 doi:10.1038/nature04141.

844 Barros, A. P., and T. J. Lang (2003), Monitoring the monsoon in the Himalayas: Observations
845 in Central Nepal, June 2001, *Monthly Weather Review*, *131*(7), 1408-1427. doi:10.1175/1520-
846 0493(2003)131<1408:MTMITH>2.0.CO;2.

847 Barros, A. P., G. Kim, E. Williams, and S. W. Nesbitt (2004), Probing orographic controls in
848 the Himalayas during the monsoon using satellite imagery, *Natural Hazards and Earth*
849 *System Sciences*, *4*(1), 29-51. doi:10.5194/nhess-4-29-2004.

850 Barros, A. P., S. Chiao, T. J. Lang, D. Burbank, and J. Putkonen (2006), From weather to
851 climate - Seasonal and interannual variability of storms and implications for erosion processes

852 in the Himalaya, *Special Paper 398: Tectonics, Climate, and Landscape Evolution*, *398*(0),
853 17-38. doi:10.1130/2006.2398(02).

854 Barry, R. G., and R. J. Chorley (2003), *Atmosphere, Weather, and Climate*, 421 pp.,
855 Routledge, London.

856 Bergström, S. (1976), Development and application of a conceptual runoff model for
857 Scandinavian catchments*Rep.*, Swedish Meteorological and Hydrological Institute (SMHI)
858 Norrköping.

859 Bergström, S. (1992), The HBV model - its structure and applications*Rep.*, 35 pp, Swedish
860 Meteorological and Hydrological Institute (SMHI), , Norrköping.

861 Berthier, E., Y. Arnaud, R. Kumar, S. Ahmad, P. Wagnon, and P. Chevallier (2007), Remote
862 sensing estimates of glacier mass balances in the Himachal Pradesh (Western Himalaya,
863 India), *Remote Sensing of Environment*, *108*(3), 327-338. doi:10.1016/j.rse.2006.11.017.

864 Bhambri, R., and T. Bolch (2009), Glacier mapping: a review with special reference to the
865 Indian Himalayas, *Progress in Physical Geography*, *33*(5), 672-704.
866 doi:10.1177/0309133309348112

867 Böhner, J., and O. Antonic (2009), Chapter 8 Land-Surface Parameters Specific to Topo-
868 Climatology, in *Developments in Soil Science*, edited by H. Tomislav and I. R. Hannes, pp.
869 195-226, Elsevier.

870 Bookhagen, B., and D. W. Burbank (2006), Topography, relief, and TRMM-derived rainfall
871 variations along the Himalaya, *Geophysical Research Letters*, *33*(8), L08405.
872 doi:10.1029/2006GL026037.

873 Bookhagen, B., and D. W. Burbank (2010), Toward a complete Himalayan hydrological
874 budget: Spatiotemporal distribution of snowmelt and rainfall and their impact on river
875 discharge, *Journal of Geophysical Research*, *115*, F03019. doi:10.1029/2009JF001426.

876 Bookhagen, B., R. C. Thiede, and M. R. Strecker (2005), Abnormal monsoon years and their
877 control on erosion and sediment flux in the high, arid northwest Himalaya, *Earth and*
878 *Planetary Science Letters*, *231*(1-2), 131-146. doi:10.1016/j.epsl.2004.11.014.

879 Braun, L. N., W. Grabs, and B. Rana (1993), Application of a Conceptual Precipitation-
880 Runoff Model in the Langtang Khola Basin, Nepal Himalaya, paper presented at IAHS Publ.,
881 Wallingford, UK.

882 Brock, B. W., C. Mihalcea, M. P. Kirkbride, G. Diolaiuti, M. E. J. Cutler, and C. Smiraglia
883 (2010), Meteorology and surface energy fluxes in the 2005-2007 ablation seasons at the
884 Miage debris-covered glacier, Mont Blanc Massif, Italian Alps, *Journal of Geophysical*
885 *Research*, *115*(D9), 1-16. doi:10.1029/2009JD013224.

886 Brubaker, K., A. Rango, and W. Kustas (1996), Incorporating Radiation Inputs Into the
887 Snowmelt Runoff Model, *Hydrological Processes*, *10*(10), 1329-1343.
888 doi:10.1002/(SICI)1099-1085(199610)10:10<1329::AID-HYP464>3.0.CO;2-W.

889 Cleugh, H., R. Leuning, Q. Mu, and S. Running (2007), Regional evaporation estimates from
890 flux tower and MODIS satellite data, *Remote Sensing of Environment*, *106*(3), 285-304.
891 doi:10.1016/j.rse.2006.07.007.

892 Coll, C., V. Caselles, J. Galve, E. Valor, R. Niclos, J. Sanchez, and R. Rivas (2005), Ground
893 measurements for the validation of land surface temperatures derived from AATSR and
894 MODIS data, *Remote Sensing of Environment*, *97*(3), 288-300. doi:10.1016/j.rse.2005.05.007.

895 Craddock, W. H., D. W. Burbank, B. Bookhagen, and E. J. Gabet (2007), Bedrock channel
896 geometry along an orographic rainfall gradient in the upper Marsyandi River valley in central
897 Nepal, *Journal of Geophysical Research-Earth Surface*, *112*, 17pp.
898 doi:10.1029/2006JF000589.

899 Dinku, T., S. Chidzambwa, P. Ceccato, S. J. Connor, and C. F. Ropelewski (2008), Validation
900 of high-resolution satellite rainfall products over complex terrain, *International Journal of*
901 *Remote Sensing*, *29*(14), 4097-4110. doi:10.1080/01431160701772526.

902 Dozier, J., and S. G. Warren (1982), Effect of viewing angle on the infrared brightness
903 temperature of snow, *Water Resources Research*, *18*(5), 1424-1434. doi:
904 10.1029/WR018i005p01424

905 Dozier, J., T. H. Painter, K. Rittger, and J. E. Frew (2008), Time-space continuity of daily
906 maps of fractional snow cover and albedo from MODIS, *Adv. Wat. Resour.*, *31*(11), 1515-
907 1526. doi:Doi 10.1016/J.Advwatres.2008.08.011.

908 Dury, G. H. (1981), *An Introduction to Environmental Systems*, Heinemann, Exeter, New
909 Hampshire.

910 Einfalt, T., and S. Michaelides (2008), Quality control of precipitation data, in *Precipitation:*
911 *Advances in Measurement, Estimation and Prediction*, edited by S. Michaelides, pp. 101-126,
912 Springer, Berlin Heidelberg.

913 FAO (2009), Land Cover Map of Himalaya Region, edited, Food and Agriculture
914 Organization of the United Nations (FAO), Rome.

915 Farr, T. G., et al. (2007), The Shuttle Radar Topography Mission, *Reviews of Geophysics*,
916 *45*(2), 1-33. doi:10.1029/2005RG000183.

917 Fisher, G. B., B. Bookhagen, and C. B. Amos (2013), Channel planform geometry and slopes
918 from freely available high-spatial resolution imagery and DEM fusion: Implications for
919 channel width scalings, erosion proxies, and fluvial signatures in tectonically active
920 landscapes, *Geomorphology*, *194*(0), 46-56. doi:10.1016/j.geomorph.2013.04.011.

921 Franz, K. J., P. Butcher, and N. K. Ajami (2010), Addressing snow model uncertainty for
922 hydrologic prediction, *Advances in Water Resources*, *33*(8), 820-832.
923 doi:10.1016/j.advwatres.2010.05.004.

924 Frey, H., F. Paul, and T. Strozzi (2012), Compilation of a glacier inventory for the western
925 Himalayas from satellite data: methods, challenges, and results, *Remote Sensing of*
926 *Environment*, *124*(0), 832-843. doi:10.1016/j.rse.2012.06.020.

927 Fritsch, F. N., and R. E. Carlson (1980), Monotone Piecewise Cubic Interpolation, *SIAM*
928 *Journal on Numerical Analysis*, *7*(2), 238-246. doi:10.1137/0717021.

929 Gafurov, A., and A. Bárdossy (2009), Cloud removal methodology from MODIS snow cover
930 product, *Hydrology and Earth System Sciences*, *13*(7), 1361-1373. doi:10.5194/hess-13-1361-
931 2009.

932 Gurtz, J., A. Baltensweiler, and H. Lang (1999), Spatially distributed hydrotope-based
933 modelling of evapotranspiration and runoff in mountainous basins, *Hydrological Processes*,
934 *13*(17), 2751-2768. doi:10.1002/(SICI)1099-1085(19991215)13:17<2751::AID-
935 HYP897>3.0.CO;2-O.

936 Hall, D. K., and G. A. Riggs (2007), Accuracy assessment of the MODIS snow products,
937 *Hydrological Processes*, *21*(12), 1534-1547. doi:10.1002/hyp.6715.

938 Hall, D. K., G. A. Riggs, and V. V. Salomonson (1995), Development of methods for
939 mapping global snow cover using moderate resolution imaging spectroradiometer data,
940 *Remote Sensing of Environment*, *54*(2), 127-140. doi:10.1016/0034-4257(95)00137-P.

941 Hall, D. K., G. A. Riggs, V. V. Salomonson, N. E. DiGirolamo, and K. J. Bayr (2002),
942 MODIS snow-cover products, *Remote Sensing of Environment*, *83*(1-2), 181-194.
943 doi:10.1016/S0034-4257(02)00095-0.

944 He, Z. H., J. Parajka, F. Q. Tian, and G. Bl√∂schl (2014), Estimating degree-day factors from
945 MODIS for snowmelt runoff modeling, *Hydrol. Earth Syst. Sci.*, *18*(12), 4773-4789.
946 doi:10.5194/hess-18-4773-2014.

947 Hobley, D. E. J., H. D. Sinclair, and S. M. Mudd (2012), Reconstruction of a major strom
948 event from its geomorphic signature: The Ladakh cloudburst, 6 August 2010., *Geology*, *40*(6),
949 483-486. doi:10.1130/G32935.1.

950 Hock, R. (1999), A distributed temperature-index ice- and snowmelt model including
951 potential direct solar radiation, *Journal of Glaciology*, *45*(149), 101-111.

952 Hock, R. (2003), Temperature index melt modelling in mountain areas, *Journal of Hydrology*,
953 *282*(1-4), 104-115. doi:10.1016/S0022-1694(03)00257-9.

954 Huffman, G. J., R. F. Adler, D. T. Bolvin, G. Gu, E. J. Nelkin, K. P. Bowman, Y. Hong, E. F.
955 Stocker, and D. B. Wolff (2007), The TRMM Multisatellite Precipitation Analysis (TMPA):
956 Quasi-Global, Multiyear, Combined-Sensor Precipitation Estimates at Fine Scales, *J.*
957 *Hydromet.*, *8*(1), 38-38. doi:http://dx.doi.org/10.1175/JHM560.1

958 Hüsler, F., T. Jonas, S. Wunderle, and S. Albrecht (2012), Validation of a modified snow
959 cover retrieval algorithm from historical 1-km AVHRR data over the European Alps, *Remote*
960 *Sensing of Environment*, *121*(0), 497-515. doi:10.1016/j.rse.2012.02.018.

961 Huss, M., D. Farinotti, A. Bauder, and M. Funk (2008), Modelling runoff from highly
962 glacierized alpine drainage basins in a changing climate, *Hydrological Processes*, *22*(19),
963 3888-3902. doi:10.1002/hyp.7055.

964 Immerzeel, W., L. P. H. van Beek, and M. F. P. Bierkens (2010), Climate change will affect
965 the Asian water towers, *Science*, *328*(5984), 1382-1385. doi:10.1126/science.1183188.

966 Immerzeel, W., F. Pellicciotti, and A. B. Shrestha (2012), Glaciers as a Proxy to Quantify the
967 Spatial Distribution of Precipitation in the Hunza Basin, *Mountain Research and*
968 *Development*, *32*(1), 30-38. doi:10.1659/mrd-journal-d-11-00097.1.

969 Immerzeel, W., P. Droogers, S. Dejong, and M. Bierkens (2009), Large-scale monitoring of
970 snow cover and runoff simulation in Himalayan river basins using remote sensing, *Remote*
971 *Sensing of Environment*, *113*(1), 40-49. doi:10.1016/j.rse.2008.08.010.

972 IPCC (2014), *Climate Change 2014: Impacts, Adaptation, and Vulnerability. Part A: Global*
973 *and Sectoral Aspects. Contribution of Working Group II to the Fifth Assessment Report of the*
974 *Intergovernmental Panel on Climate Change [Field, C.B., V.R. Barros, D.J. Dokken, K.J.*
975 *Mach, M.D. Mastrandrea, T.E. Bilir, M. Chatterjee, K.L. Ebi, Y.O. Estrada, R.C. Genova, B.*
976 *Girma, E.S. Kissel, A.N. Levy, S. MacCracken, P.R. Mastrandrea, and L.L. White (eds.)]*,
977 1132 pp., Cambridge University Press, Cambridge, United Kingdom and New York, NY,
978 USA.

979 Jeelani, G., J. J. Feddema, C. J. van der Veen, and L. Stearns (2012), Role of snow and glacier
980 melt in controlling river hydrology in Liddar watershed (western Himalaya) under current and
981 future climate, *Water Resources Research*, *48*(12), W12508. doi:10.1029/2011wr011590.

982 Jin, J., X. Gao, S. Sorooshian, Z.-L. Yang, R. Bales, R. E. Dickinson, S.-F. Sun, and G.-X.
983 Wu (1999), One-dimensional snow water and energy balance model for vegetated surfaces,
984 *Hydrological Processes*, *13*(14-15), 2467-2482. doi:10.1002/(sici)1099-
985 1085(199910)13:14/15<2467::aid-hyp861>3.0.co;2-j.

986 Jolliffe, I. T., and D. B. Stephenson (2003), *Forecast Verification: A Practitioner's Guide in*
987 *Atmospheric Science*, 240 pp., Wiley, Hoboken, NJ.

988 Kääb, A., E. Berthier, C. Nuth, J. Gardelle, and Y. Arnaud (2012), Contrasting patterns of
989 early twenty-first-century glacier mass change in the Himalayas, *Nature*, *488*(7412), 495-498.
990 doi:10.1038/nature11324.

991 Klein, A. G., and A. C. Barnett (2003), Validation of daily MODIS snow cover maps of the
992 Upper Rio Grande River Basin for the 2000-2001 snow year, *Remote Sensing of Environment*,
993 *86*(2), 162-176. doi:10.1016/S0034-4257(03)00097-X.

994 Kumar, M., D. Marks, J. Dozier, M. Reba, and A. Winstral (2013), Evaluation of distributed
995 hydrologic impacts of temperature-index and energy-based snow models, *Advances in Water*
996 *Resources*, *56*(0), 77-89. doi:http://dx.doi.org/10.1016/j.advwatres.2013.03.006.

997 Lang, H., and L. Braun (1990), On the information content of air temperature in the context of
998 snow melt estimation, in *Hydrology of Mountainous Areas*, edited by L. Molar, pp. 347–354,
999 IAHS, Zürich.

1000 Leopold, L., and T. Maddock (1953), The hydraulic geometry of stream channels and some
1001 physiographic implications, *United States Geological Survey, Professional Paper 252*.

1002 Li, X., and M. W. Williams (2008), Snowmelt runoff modelling in an arid mountain
1003 watershed, Tarim Basin, China, *Hydrological Processes*, *22*(19), 3931–3940.
1004 doi:10.1002/hyp.7098.

1005 Lundquist, J. D., and D. R. Cayan (2007), Surface temperature patterns in complex terrain:
1006 Daily variations and long-term change in the central Sierra Nevada, California, *Journal of*
1007 *Geophysical Research*, *112*(D11), 1-15. doi:10.1029/2006JD007561.

1008 Martinec, J. (1975), Snowmelt - Runoff model for stream flow forecasts, *Nordic Hydrology*,
1009 *6*(3), 145-154. doi:10.2166/nh.1975.010.

1010 Mattson, L. E., J. S. Gardner, and G. J. Young (1993), Ablation on debris covered glaciers: an
1011 example from the Rakhiot Glacier, Punjab, Himalaya., in *Snow and Glacier Hydrology.*
1012 *International Symposium*, edited by G. J. Young, pp. 289-296, Proceedings. International
1013 Association of Hydrological Sciences. IAHS/AISH Publication, Kathmandu.

1014 Maussion, F., D. Scherer, R. Finkelnburg, J. Richters, W. Yang, and T. Yao (2011), WRF
1015 simulation of a precipitation event over the Tibetan Plateau, China - an assessment using
1016 remote sensing and ground observations, *Hydrol. Earth Syst. Sci.*, *15*(6), 1795-1817.
1017 doi:10.5194/hess-15-1795-2011.

1018 Minder, J. R., P. W. Mote, and J. D. Lundquist (2010), Surface temperature lapse rates over
1019 complex terrain: Lessons from the Cascade Mountains, *Journal of Geophysical Research*,
1020 *115*, D14122, 14113 pp. doi:10.1029/2009JD013493.

1021 Molotch, N. P., and D. Norte (2009), Reconstructing snow water equivalent in the Rio Grande
1022 headwaters using remotely sensed snow cover data and a spatially distributed snowmelt
1023 model, *Hydrological Processes*, *1089*, 1076-1089. doi:10.1002/hyp.7206.

1024 Monteith, J. L. (1965), Evaporation and environment, in *Symposia of the Society for*
1025 *Experimental Biology*, edited, pp. 205-234.

1026 Mu, Q., M. Zhao, and S. W. Running (2011), Improvements to a MODIS global terrestrial
1027 evapotranspiration algorithm, *Remote Sensing of Environment*, *115*(8), 1781-1800.
1028 doi:10.1016/j.rse.2011.02.019.

1029 Mu, Q., F. A. Heinsch, M. Zhao, and S. W. Running (2007), Development of a global
1030 evapotranspiration algorithm based on MODIS and global meteorology data, *Remote Sensing*
1031 *of Environment*, *111*(4), 519-536. doi:10.1016/J.Rse.2007.04.015.

1032 Mu, Q., L. A. Jones, J. S. Kimball, K. C. McDonald, and S. W. Running (2009), Satellite
1033 assessment of land surface evapotranspiration for the pan-Arctic domain, *Water Resources*
1034 *Research*, *45*(9), W09420. doi:10.1029/2008wr007189.

1035 Nash, J. E., and J. V. Sutcliffe (1970), River flow forecasting through conceptual models. Part
1036 I: a discussion of principles, *Journal of Hydrology*, *10*, 282-290. doi:10.1016/0022-
1037 1694(70)90255-6.

1038 Ohmura, A. (2001), Physical Basis for the Temperature-Based Melt-Index Method, *Journal of*
1039 *Applied Meteorology*, *40*(4), 753-761. doi:10.1175/1520-
1040 0450(2001)040%3C0753:PBFTTB%3E2.0.CO;2.

1041 Pan, M., H. Li, and E. Wood (2010), Assessing the skill of satellite-based precipitation
1042 estimates in hydrologic applications, *Water Resources Research*, *46*(9), 1-10.
1043 doi:10.1029/2009WR008290.

1044 Pandit, M. K., M. S. Bisht, J. P. Bhatt, S. K. Pattanayak, D. C. Nautiyal, and R. Mehta (2010),
1045 Environmental Impact Assessment of Luhri HydroElectric Project, Himachal Pradesh*Rep.*,
1046 Centre for inter-disciplinary studies of mountain & hill environment, Delhi.

1047 Parajka, J., and G. Blöschl (2006), Validation of MODIS snow cover images over Austria,
1048 *Hydrology and Earth System Sciences Discussions*, *3*(4), 1569-1601. doi:10.5194/hess-10-
1049 679-2006.

1050 Pellicciotti, F., T. Raschle, T. Huerlimann, M. Carenzo, and P. Burlando (2011),
1051 Transmission of solar radiation through clouds on melting glaciers: a comparison of
1052 parameterizations and their impact on melt modelling, *Journal of Glaciology*, *57*(202), 367-
1053 381. doi:10.3189/002214311796406013.

1054 Pellicciotti, F., B. Brock, U. Strasser, P. Burlando, M. Funk, and J. Corripio (2005), An
1055 enhanced temperature-index glacier melt model including the shortwave radiation balance:
1056 development and testing for Haut Glacier d'Arolla, Switzerland, *Journal of Glaciology*,
1057 *51*(175), 573-587. doi:10.3189/172756505781829124.

1058 Preparata, F. R., and M. I. Shamos (1985), *Computational Geometry: An Introduction*,
1059 Springer-Verlag, New York.

1060 Prince, S. D., S. J. Goetz, R. O. Dubayah, K. P. Czajkowski, and M. Thawley (1998),
1061 Inference of surface and air temperature, atmospheric precipitable water and vapor pressure
1062 deficit using Advanced Very High-Resolution Radiometer satellite observations: comparison
1063 with field observations, *Journal of Hydrology*, *213*(1-4), 230-249. doi:10.1016/S0022-
1064 1694(98)00210-8.

1065 Racoviteanu, A. E., R. Armstrong, and M. W. Williams (2013), Evaluation of an ice ablation
1066 model to estimate the contribution of melting glacier ice to annual discharge in the Nepalese
1067 Himalaya, *Water Resources Research*, *49*, 5117–5133. doi:10.1002/wrcr.20370.

1068 Ragettli, S., F. Pellicciotti, R. Bordoy, and W. W. Immerzeel (2013), Sources of uncertainty
1069 in modeling the glacio-hydrological response of a Karakoram watershed to climate change,
1070 *Water Resources Research*, *49*, 6048–6066. doi:10.1002/wrcr.20450.

1071 Rango, A., and J. Martinec (1995), Revisiting the Degree-Day Method for Snowmelt
1072 Computations, *Water Resources Bulletin*, *31*(4), 657-669. doi:10.1111/j.1752-
1073 1688.1995.tb03392.x.

1074 Reid, T. D., and B. W. Brock (2010), An energy-balance model for debris-covered glaciers
1075 including heat conduction through the debris layer, *Journal of Glaciology*, *56*(199), 903-916.
1076 doi:10.3189/002214310794457218.

1077 Rittger, K., T. H. Painter, and J. Dozier (2013), Assessment of methods for mapping snow
1078 cover from MODIS, *Advances in Water Resources*, *51*, 367-380.
1079 doi:10.1016/j.advwatres.2012.03.002.

1080 Rodell, M., I. Velicogna, and J. S. Famiglietti (2009), Satellite-based estimates of
1081 groundwater depletion in India, *Nature*, *460*(7258), 999-1002. doi:10.1038/nature08238.

1082 Salomonson, V., and Apple (2004), Estimating fractional snow cover from MODIS using the
1083 normalized difference snow index, *Remote Sensing of Environment*, *89*(3), 351-360.
1084 doi:10.1016/j.rse.2003.10.016.

1085 Sapiano, M. R. P. (2009), An evaluation of high resolution precipitation products at low
1086 resolution, *International Journal of Climatology*, *30*(9), 1416-1422. doi:10.1002/joc.1961.

1087 Scherler, D., B. Bookhagen, and M. R. Strecker (2011), Spatially variable response of
1088 Himalayan glaciers to climate change affected by debris cover, *Nature Geoscience*, *4*, 156–
1089 159. doi:10.1038/ngeo1068.

1090 Schmugge, T. J., W. P. Kustas, J. C. Ritchie, T. J. Jackson, and A. Rango (2002), Remote
1091 sensing in hydrology, *Advances in Water Resources*, *25*(8-12), 1367-1385.
1092 doi:10.1016/S0309-1708(02)00065-9.

1093 Schulze, K., M. Hunger, and P. Döll (2005), Simulating river flow velocity on global scale,
1094 *Adv. Geosci.*, *5*, 133-136. doi:10.5194/adgeo-5-133-2005.

1095 Schwanghart, W., and D. Scherler (2014), Short Communication: TopoToolbox 2 -
1096 MATLAB-based software for topographic analysis and modeling in Earth surface sciences,
1097 *Earth Surf. Dynam.*, *2*(1), 1-7. doi:10.5194/esurf-2-1-2014.

1098 Schwarze, R., W. Droege, and K. Opherden (1999), Regional analysis and modelling of
1099 groundwater runoff components from catchments in hard rock areas, in *Regionalisation in*
1100 *Hydrology*, edited by B. Diekkrüger, M. J. Kirkby and U. Schröder, pp. 221–232, IAHS
1101 Press, Wallingford, UK.

1102 Singh, P., and N. Kumar (1997), Effect of orography on precipitation in the western
1103 Himalayan region, *Journal of Hydrology*, *199*(1-2), 183-206. doi:10.1016/S0022-
1104 1694(96)03222-2.

1105 Singh, P., and S. K. Jain (2002), Snow and glacier melt in the Satluj River at Bhakra Dam in
1106 the western Himalayan region, *Hydrological Sciences Journal*, *47*(1), 93-106.
1107 doi:10.1080/02626660209492910.

1108 Singh, P., and S. K. Jain (2003), Modelling of streamflow and its components for a large
1109 Himalayan basin with predominant snowmelt yields, *Hydrological Sciences Journal*, *48*(2),
1110 257-276. doi:10.1623/hysj.48.2.257.44693.

1111 Singh, P., and L. Bengtsson (2003), Effect of warmer climate on the depletion of
1112 snowcovered area in the Satluj basin in the western Himalayan region, *Hydrological Sciences*
1113 *Journal*, *48*(3), 413-425. doi:10.1623/hysj.48.3.413.45280.

1114 Sorg, A., T. Bolch, M. Stoffel, O. Solomina, and M. Beniston (2012), Climate change impacts
1115 on glaciers and runoff in Tien Shan (Central Asia), *Nature Climate Change*, *2*(10), 725-731.
1116 doi:10.1038/nclimate1592.

1117 Stephens, G. L., R. D. Cess, M. H. Zhang, P. Pilewskie, and F. P. J. Valero (1996), How
1118 Much Solar Radiation Do Clouds Absorb?, *Science*, *271*(5252), 1131.
1119 doi:10.1126/science.271.5252.1131.

1120 Swets, J. A. (1986), Form of empirical ROCs in discrimination and diagnostic tasks:
1121 Implications for theory and measurement of performance, *Psychological Bulletin*, *99*(2), 181-
1122 198. doi:10.1037/0033-2909.99.2.181.

1123 Thayyen, R. J., J. T. Gergan, and D. P. Dobhal (2007), Role of glaciers and snow cover on
1124 headwater river hydrology in monsoon regime - Micro-scale study of Din Gad catchment,
1125 Garhwal Himalaya, India, *Current Science*, *92*(3), 376-382.

1126 Tian, Y. D., C. D. Peters-Lidard, J. B. Eylander, R. J. Joyce, G. J. Huffman, R. F. Adler, K. L.
1127 Hsu, F. J. Turk, M. Garcia, and J. Zeng (2009), Component analysis of errors in satellite-
1128 based precipitation estimates, *Journal of Geophysical Research*, *114*, D24101.24101-24115.
1129 doi:10.1029/2009jd011949.

1130 Viviroli, D., J. Gurtz, and M. Zappa (2007), The Hydrological Modelling System PREVAH,
1131 in *Geographica Bernensia*, edited, Institute of Geography, University of Berne, Berne.

1132 Viviroli, D., M. Zappa, J. Gurtz, and R. Weingartner (2009), An introduction to the
1133 hydrological modelling system PREVAH and its pre- and post-processing-tools,
1134 *Environmental Modelling & Software*, *24*(10), 1209-1222.
1135 doi:10.1016/J.Envsoft.2009.04.001.

1136 Wagnon, P., et al. (2007), Four years of mass balance on Chhota Shigri Glacier, Himachal
1137 Pradesh, India, a new benchmark glacier in the western Himalaya, *Journal of Glaciology*,
1138 *53*(183), 603-611. doi:10.3189/002214307784409306.

1139 Wan, Z. (2008), New refinements and validation of the MODIS Land-Surface
1140 Temperature/Emissivity products, *Remote Sensing of Environment*, *112*(1), 59-74.
1141 doi:10.1016/j.rse.2006.06.026.

1142 Wan, Z., and J. Dozier (1996), A generalized split-window algorithm for retrieving land-
1143 surface temperature from space, *IEEE Transactions on Geoscience and Remote Sensing*,
1144 *34*(4), 892-905. doi:10.1109/36.508406.

1145 Wan, Z., Y. Zhang, and Q. Zhang (2004), Quality assessment and validation of the MODIS
1146 global land surface temperature, *International Journal of Remote Sensing*, *25*(1), 261-274.
1147 doi:10.1080/0143116031000116417.

1148 WDI (2010), World Bank, World Development Indicators*Rep.*, University of Manchester,
1149 Manchester.

1150 Winiger, M., M. Gumpert, and H. Yamout (2005), Karakorum-Hindukush-western Himalaya:
1151 assessing high-altitude water resources, *Hydrological Processes*, *19*(12), 2329-2338.
1152 doi:10.1002/hyp.5887.

1153 Wulf, H., B. Bookhagen, and D. Scherler (2010), Seasonal precipitation gradients and their
1154 impact on fluvial sediment flux in the Northwest Himalaya, *Geomorphology*, *118*(1-2), 13-21.
1155 doi:10.1016/J.Geomorph.2009.12.003.

1156 Wulf, H., B. Bookhagen, and D. Scherler (2012), Climatic and geologic controls on
1157 suspended sediment flux in the Sutlej River Valley, western Himalaya, *Hydrol. Earth Syst.*
1158 *Sci.*, *16*(7), 2193-2217. doi:10.5194/hess-16-2193-2012.

1159 Zhang, L., F. Su, D. Yang, Z. Hao, and K. Tong (2013), Discharge regime and simulation for
1160 the upstream of major rivers over Tibetan Plateau, *Journal of Geophysical Research:*
1161 *Atmospheres*. doi:10.1002/jgrd.50665.

1162

1163

1164

# Tables

**Table 1:** Topographic, land cover, and hydrological characteristics of the modeled catchments

| | Catchments[a] | Topography | | | | | | | Land cover | | | Hydrology | |
|---|---|---|---|---|---|---|---|---|---|---|---|---|---|
| | | Area | Elevation | | | Relief | Location | | Bare ground | Vegetation | Glacier | Snow cover | Runoff |
| | | | min | mean | max | [km/ | Lat | Lon | area | area | area | area | [m |
| | | [km$^2$] | [km] | [km] | [km] | 5 km] | [°] | [°] | [%] | [%] | [%] | [%] | yr$^{-1}$ m$^{-2}$] |
| *Tributaries* | Ganvi (a) | 117 | 1.6 | 3.4 | 5.6 | 2.58 | 31.55 | 77.76 | 33.3 | 62.5 | 4.1 | 25.6 | 1.25 |
| | Wanger (b) | 264 | 2.5 | 4.4 | 5.7 | 2.24 | 31.62 | 78.02 | 69.1 | 16.1 | 14.8 | 55.4 | 1.59 |
| | Baspa (c) | 989 | 2.5 | 4.7 | 6.4 | 2.21 | 31.42 | 78.26 | 57.1 | 23.8 | 19.1 | 54.8 | 1.16 |
| | Spiti (d) | 12,477 | 2.6 | 5.0 | 6.7 | 1.68 | 31.81 | 78.64 | 92.6 | 1.6 | 5.9 | 38.4 | 0.23 |
| *Sutlej River at* | Namgia (e) | 30,950 | 2.6 | 4.8 | 7.2 | 0.93 | 31.81 | 78.65 | 91.1 | 7.0 | 1.9 | 19.8 | 0.06 |
| | Karoo (f) | 46,025 | 2.2 | 4.8 | 7.2 | 1.21 | 31.59 | 78.36 | 90.9 | 5.9 | 3.2 | 26.1 | 0.14 |
| | Powari (g) | 46,291 | 1.9 | 4.8 | 7.2 | 1.22 | 31.52 | 78.27 | 90.7 | 6.1 | 3.2 | 26.1 | 0.15 |
| | Wangtoo (h) | 48,316 | 1.5 | 4.8 | 7.2 | 1.27 | 31.56 | 77.98 | 89.3 | 7.1 | 3.6 | 26.9 | 0.20 |
| | Bhakra (i) | 54,926 | 0.4 | 4.4 | 7.2 | 1.30 | 31.41 | 76.43 | 81.7 | 15.1 | 3.2 | 24.1 | 0.23 |

[a] Labels in parenthesis refer to the gauging station of each catchment as indicated in Figure 1.

**Table 2:** Values of calibrated tunable and constant model parameters for each catchment.

| Catchments | | Tunable model parameter | | | | | | | Constant model parameter | | | |
|---|---|---|---|---|---|---|---|---|---|---|---|---|
| | | $srf_S$ [mm $m^2$ $W^{-1}$ $day^{-1}$] | $tf_S$ [mm $°C^{-1}$ $day^{-1}$] | $srf_G$ [mm $m^2$ $W^{-1}$ $day^{-1}$] | $tf_G$ [mm $°C^{-1}$ $day^{-1}$] | $SI_{MAX}$ [mm] | $SG1_{MAX}$ [mm] | $PERC_{MAX}$ [mm $day^{-1}$] | K0 [day] | K1 [day] | K2 [day] | K3 [day] |
| *Tributaries* | Ganvi | 0.150 | 1.72 | 0.482 | 0.50 | 2.5 | 20.7 | 6.2 | 0.4 | 3.1 | 31.3 | 104.2 |
| | Wanger | 0.088 | 6.44 | 0.484 | 1.79 | 6.5 | 32.5 | 13.9 | 0.4 | 3.1 | 31.3 | 104.2 |
| | Baspa | 0.093 | 5.21 | 0.313 | 0.76 | 23.5 | 84.2 | 16.9 | 0.4 | 3.1 | 31.3 | 104.2 |
| | Spiti | 0.022 | 2.73 | 0.160 | 0.24 | 54.5 | 266.9 | 79.8 | 0.4 | 3.1 | 31.3 | 104.2 |
| *Sutlej River at* | Namgia | 0.009 | 0.89 | 0.062 | 1.34 | 35.0 | 183.5 | 29.8 | 0.4 | 3.1 | 31.3 | 104.2 |
| | Karoo | 0.021 | 2.54 | 0.138 | 0.28 | 140.1 | 667.1 | 111.1 | 0.4 | 3.1 | 31.3 | 104.2 |
| | Powari | 0.019 | 2.62 | 0.127 | 0.22 | 132.8 | 673.4 | 125.5 | 0.4 | 3.1 | 31.3 | 104.2 |
| | Wangtoo | 0.025 | 3.09 | 0.165 | 0.52 | 150.0 | 725.7 | 170.3 | 0.4 | 3.1 | 31.3 | 104.2 |
| | Bhakra | 0.019 | 1.80 | 0.119 | 0.38 | 158.7 | 794.8 | 232.0 | 0.4 | 3.1 | 31.3 | 104.2 |

1174 **Table 3:** Evaluation of air temperature datasets based on linear regressions with weather-
1175 station records

| Approach | Method | Regression parameter | | | | | |
|---|---|---|---|---|---|---|---|
| | | $r^2$ | | *rmse* [°C] | | *fit slope* | |
| [#] | | day | night | day | night | day | night |
| 1 | Seasonally constant lapse rate (-6.5°C/km) | 0.84 | 0.90 | 3.72 | 3.10 | 0.83 | 0.94 |
| 2 | Seasonally variable day- and night lapse rate | 0.89 | 0.92 | 2.95 | 2.51 | 0.90 | 0.90 |
| 3 | Scaled MODIS LST data | 0.91 | 0.94 | 2.80 | 2.45 | 1.02 | 0.99 |

1176

1177

**Table 4:** Tunable and constant parameters of the melt and runoff response routine

| Parameter | Description | Unit | Range[a] | Value[a] | Estimation method |
|---|---|---|---|---|---|
| *Snow and glacier routine* | | | | | |
| $srf_S$ | shortwave radiation factor for snow melt | [mm $W^{-1}$ $m^2$ $day^{-1}$] | 0 - 0.129 | 0.019 | Calibration |
| $tf_S$ | empirical temperature factor for snow melt | [mm $°C^{-1}$ $day^{-1}$] | 0 - 7.75 | 1.80 | Calibration |
| $srf_G$ | shortwave radiation factor for glacial melt | [mm $W^{-1}$ $m^2$ $day^{-1}$] | 0 - 0.645 | 0.119 | Calibration |
| $tf_G$ | empirical temperature factor for glacial melt | [mm $°C^{-1}$ $day^{-1}$] | 0 - 32.28 | 0.38 | Calibration |
| *df* | Scaling factor for debris-covered ice | [dimensionless] | - | 0.7 | Azam et al. 2012[b] |
| $T_T$ | Threshold temperature | [°C] | - | 0 | Viviroli et al. 2007[c] |
| *Runoff response routine* | | | | | |
| $SI_{MAX}$ | Threshold content of the lower SUZ for generation of surface runoff (SGR) | [mm] | 0-1000 | 158.7 | Calibration |
| $SG1_{MAX}$ | Threshold content of the SG1 for generation of slow-leaking recharge | [mm] | 0-1000 | 794.8 | Calibration |
| $PERC_{MAX}$ | Maximal deep percolation rate | [mm $day^{-1}$] | 0-1000 | 232.0 | Calibration |
| *K0* | Storage time for surface runoff | [day] | - | 0.42 | Viviroli et al. 2007[c] |
| *K1* | Storage time for interflow | [day] | - | 3.13 | Viviroli et al. 2007[c] |
| *K2* | Storage time for quick groundwater flow | [day] | - | 31.25 | Viviroli et al. 2007[c] |
| *K3* | Storage time for slow groundwater flow | [day] | - | 104.16 | Viviroli et al. 2007[c] |

[a] Range and value of tunable parameters are given exemplarily for the Sutlej catchment at Bhakra.

[b] value is based on mass balance data published by *Azam et al.*, [2012]

[c] use of PREVAH-default values for the respective runoff type storage time as defined in *Viviroli et al.* [2007]

1186 **Table 5:** Comparison of our three different rainfall dataset by their Nash Sutcliffe Efficiency

1187 (NSE), relative volume error (RVE), and their mean annual catchment rainfall (Rain).

| *Rainfall datasets:* | | (1) Weather station data | | | (2) TRMM original | | | (3) TRMM re-calibrated | | | (3) Discharge sources[a] | | |
|---|---|---|---|---|---|---|---|---|---|---|---|---|---|
| | | NSE | RVE | Rain | NSE | RVE | Rain | NSE | RVE | Rain | Snow | Ice | Rain-ET |
| **Catchments** | | [-] | [%] | [mm/yr] | [-] | [%] | [mm/yr] | [-] | [%] | [mm/yr] | [%] | [%] | [%] |
| *Tributaries* | Ganvi (a) | 0.50 | -5.9 | 494 | 0.27 | 21.8 | 745 | 0.59 | 1.4 | 511 | 58 | 1 | 41 |
| | Wanger (b) | 0.55 | -2.6 | 245 | 0.54 | 12.3 | 478 | 0.68 | -2.3 | 162 | 72 | 15 | 13 |
| | Baspa (c) | 0.77 | 9.3 | 266 | 0.56 | 15.6 | 514 | 0.75 | -6.5 | 218 | 75 | 13 | 13 |
| | Spiti (d) | -7.49 | 123.6 | 273 | -0.16 | 39.0 | 152 | 0.78 | -0.2 | 31 | 67 | 22 | 11 |
| *Sutlej River at* | Namgia (e) | -107.91 | 531.8 | 392 | -36.81 | 309.9 | 237 | 0.54 | -1.6 | 50 | 42 | 19 | 39 |
| | Karoo (f) | -6.30 | 135.4 | 351 | -2.90 | 100.2 | 213 | 0.71 | 2.8 | 44 | 65 | 18 | 17 |
| | Powari (g) | -18.22 | 194.2 | 350 | -3.17 | 98.9 | 213 | 0.75 | -2.2 | 45 | 66 | 17 | 18 |
| | Wangtoo (h) | -2.60 | 99.7 | 348 | -3.16 | 84.1 | 218 | 0.72 | -3.2 | 51 | 66 | 18 | 16 |
| | Bhakra (i) | -5.24 | 96.1 | 392 | -1.99 | 68.4 | 300 | 0.72 | 1.1 | 131 | 35 | 10 | 55 |

1188

1189 [a] The discharge sources represent the modeling results for the third re-calibrated TRMM
1190 rainfall dataset, which we used to drive the hydrological model.

1191

# Figures

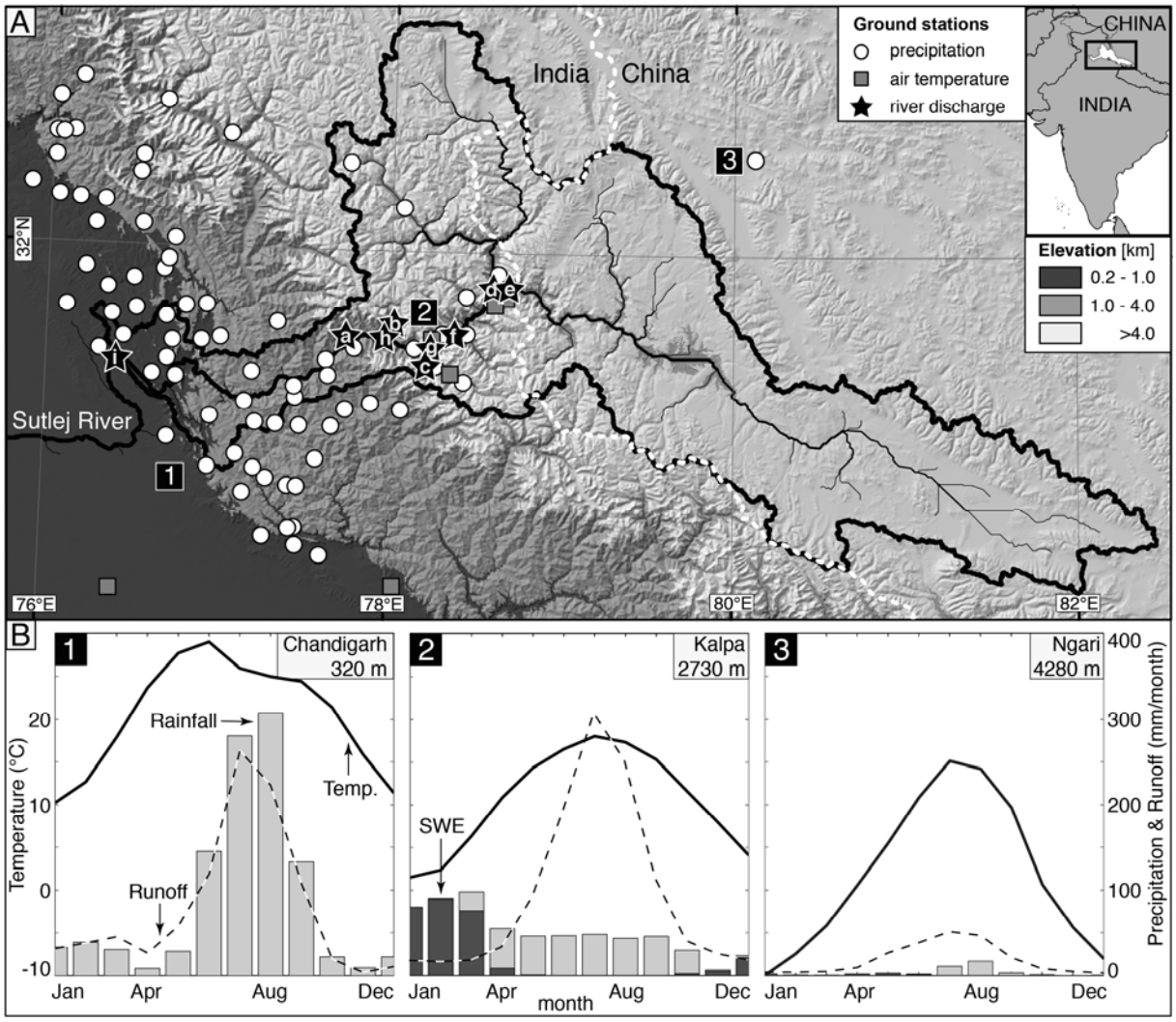


**Figure 1:** (A) Shaded relief and elevation map of the western Himalaya with inset showing map location. Black polygon outlines the Sutlej catchment and defines the hydrologic model domain; white dashed line is the international border between India and China. White circles indicate weather stations recording rainfall and partially snow water equivalent. Gray squares represent weather stations in Patiala, Dehradun, Kalpa, Rakchham, Khab and Namgia (west to east), which additionally record daily minimum and maximum temperatures. Black stars denote river-gauging stations of the Sutlej main stem and tributaries at Bhakra (i), Ganvi (a), Wangtoo (h), Wanger (b), Baspa (c), Powari (g), Karoo (f), Spiti (d), Namgia (d) (west to east, cf. Table 1). (B) Characteristic ground-station data showing mean monthly temperature, precipitation, and runoff at the Himalayan Front (1), at the Himalayan Crest (2), and at the southern Tibetan Plateau (3).

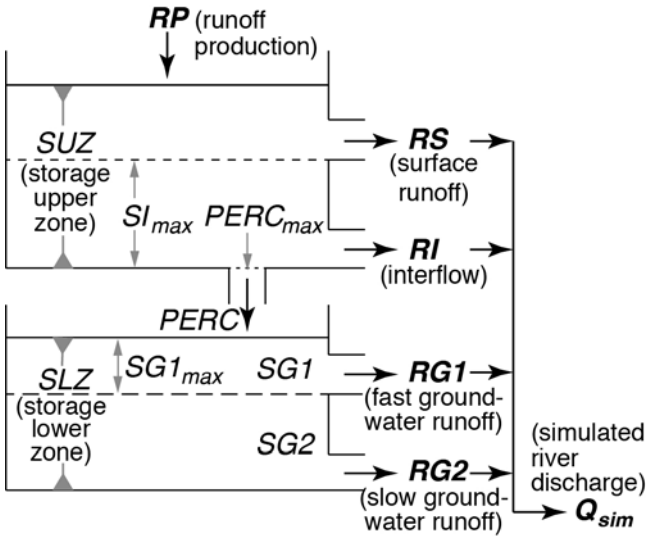


1206

1207 **Figure 2:** Schematic overview of runoff fluxes and storage modules in the hydrological model. *SG1*
1208 and *SG2* represent fast and slow-leaking groundwater storages, respectively. $SI_{max}$, $SG1_{max}$, and
1209 $PERC_{max}$ represent thresholds for the generation of surface runoff, slow groundwater runoff, and the
1210 percolation rate (*PERC*), respectively.

1211

1212

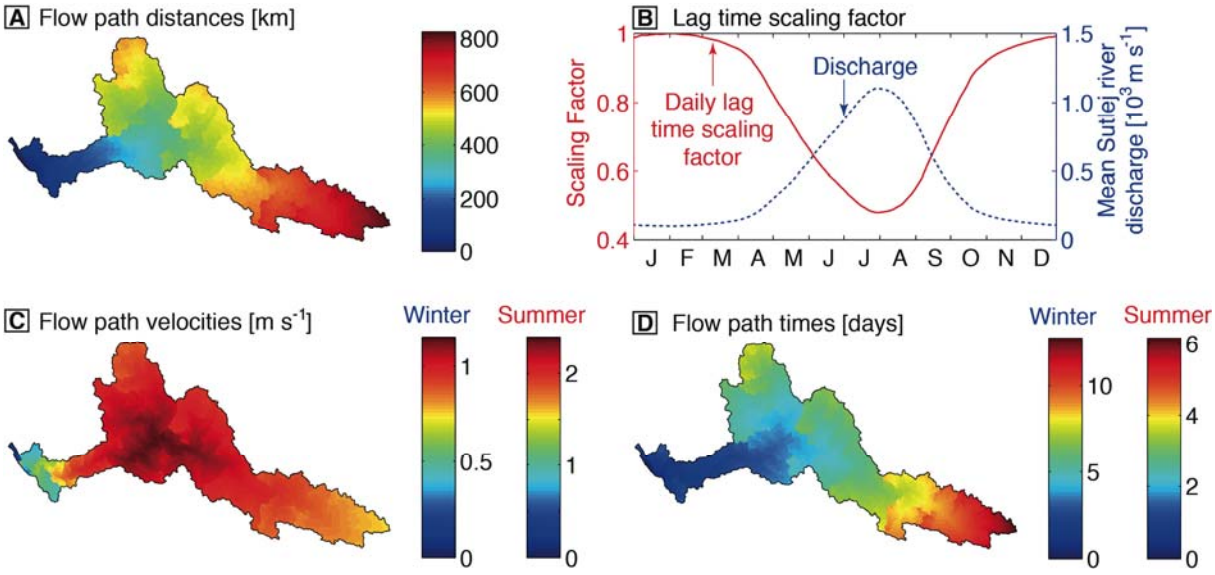


**Figure 3:** (A) Flow-path distances in km for each cell to the Sutlej River at Bhakra. (B) Lag-time scaling factor based on the annual mean discharge at Bhakra smoothed with a 50-day running window. (C) Mean-seasonal flow path velocities for the path of each cell to the Sutlej River at Bahkra. Note the generally higher flow velocities in the steep sections of the middle Sutlej. (D) Mean-seasonal flow path times.

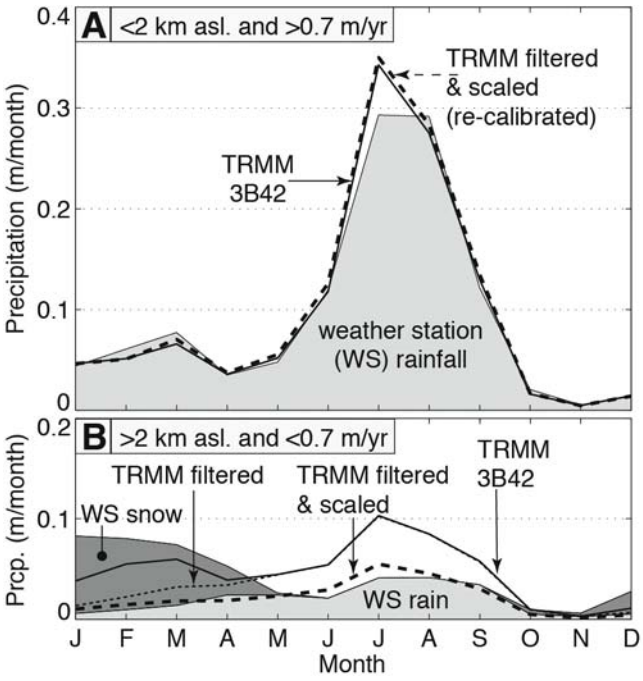


**Figure 4:** (A) Comparison of original (solid line), filtered (dotted line), and filtered & scaled (re-calibrated) (dashed line) TRMM 3B42 V7 with weather station (WS) rainfall data at 66 locations below 2000 m asl for the time period 2000 to 2012. Scaling is based on the relation between TRMM 3B42 and weather station data (Figure 5) and TRMM 3B42 data is filtered for snow cover and maximum daily temperatures below 0°C. Mean annual rainfall in this region is >0.7 m/yr. (B) Comparison of original (solid line), filtered (dotted line), and filtered & scaled (re-calibrated) (dashed line) TRMM 3B42 (2000 to 2012) with snow water equivalent (SWE) and rainfall data of 16 weather stations (WS) located above 2000 m asl, where mean annual rainfall is <0.7 m/yr.

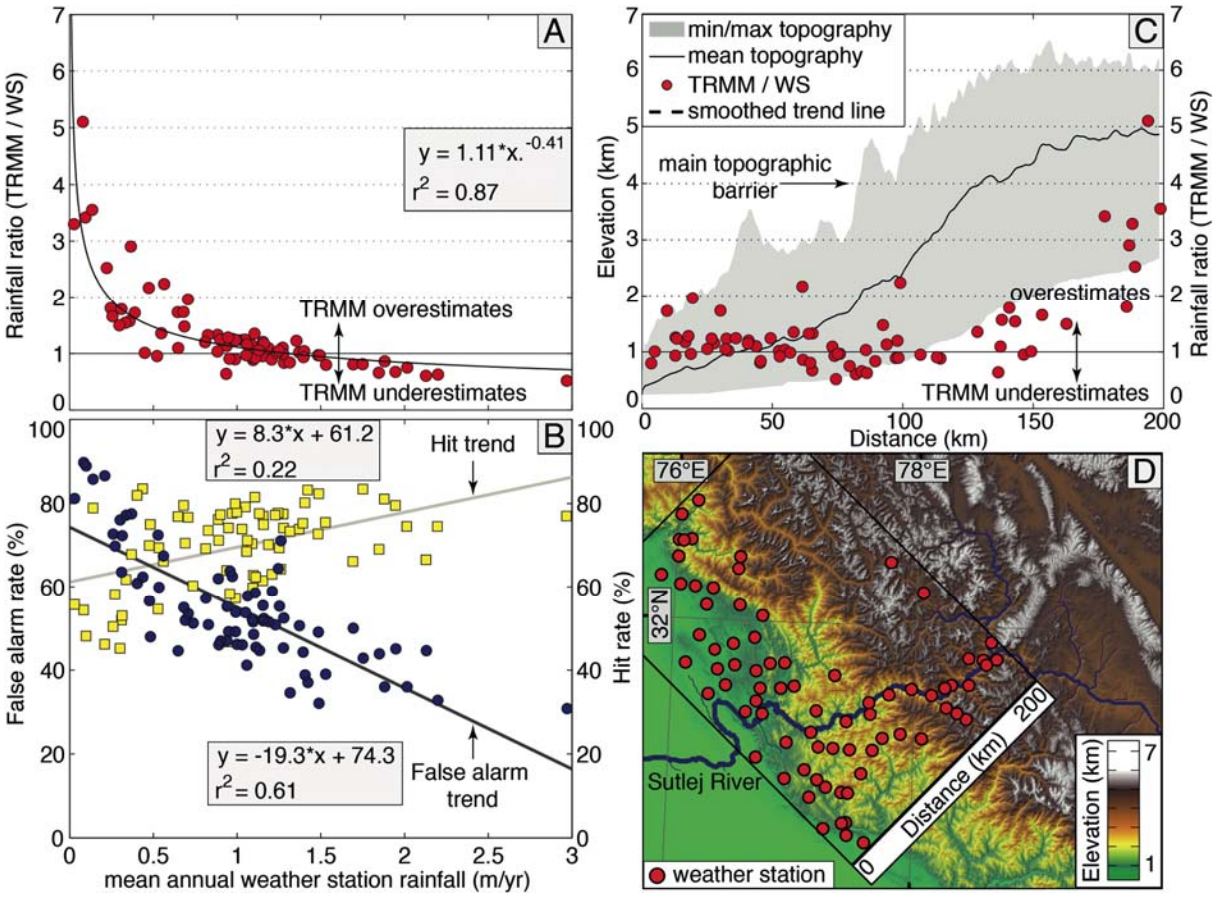


**Figure 5:** (A) Correlation of mean annual weather station (WS) rainfall data versus the ratio of mean annual TRMM 3B42 to WS data for the period 2000 to 2012. This rainfall ratio indicates a scaling factor by which TRMM over (>1) or underestimates (<1) weather station records. (B) Analysis of TRMM 3B42 data regarding its probability of detection and misinterpretation of daily rainfall at weather stations. (C) Topographic swath profile of the western Himalaya and the mean annual precipitation ratio of TRMM 3B42 and WS records. (D) Location of weather stations and the topographic swath profile.

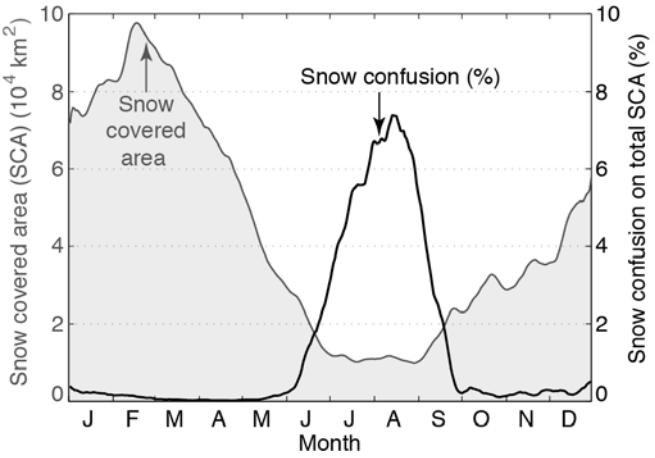


1242

1243 **Figure 6:** Mean annual (2000 to 2012) distribution of snow covered area (SCA) and the percentage of
1244 misclassified snow on total snow cover (M*D10A1). We applied a 10-day moving average filter for
1245 enhanced visibility.

1246

1247

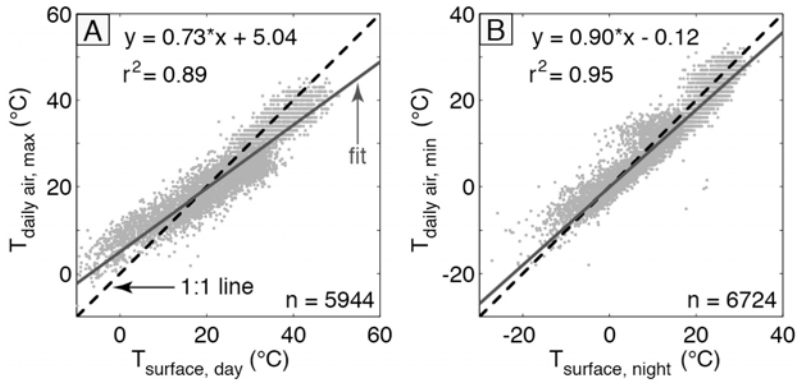


1248

1249 **Figure 7:** (A) Linear regression of daily maximum air temperatures from Kalpa, Rakchham, Namgia,
1250 Patiala, and Dehradun (cf. Figure 1) versus daytime MODIS Terra land surface temperatures (LST)
1251 weighted by the satellite sensor angle. In general, data with high residuals have higher sensor angles.
1252 (B) Same regression as in A for daily minimum temperatures versus nighttime MODIS Terra LST.
1253 Regressions for the MODIS Aqua sensor display the same trend (Figure S3). Nighttime correlation
1254 includes more data points as cloud cover at night is generally lower.

1255

1256

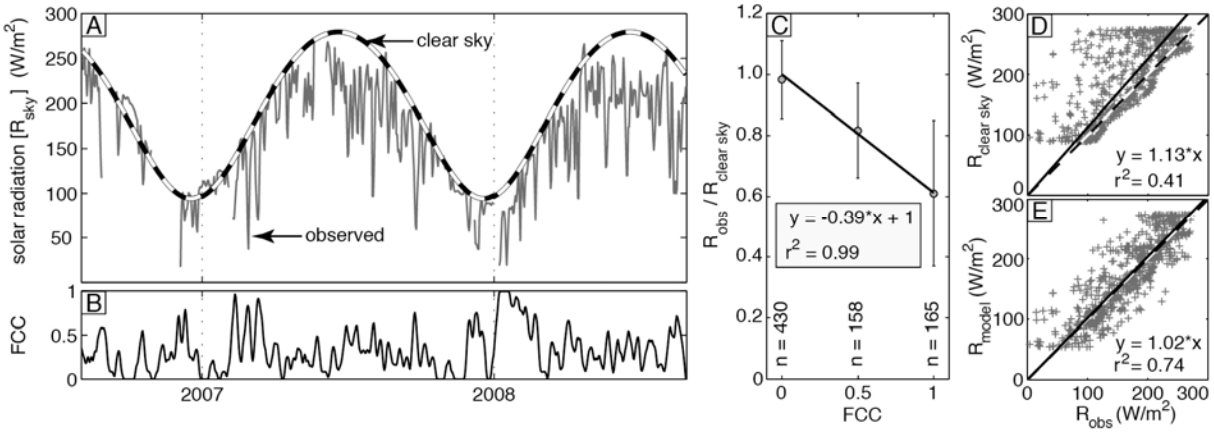


1257

1258 **Figure 8:** (A) Comparison of mean daily observed ($R_{obs}$) and computed ($R_{clear\ sky}$) incoming solar
1259 radiation from August 2006 to August 2008 at Khab (cf. Figure 1). (B) Fractional cloud cover (FCC) is
1260 derived from MODIS Aqua and Terra daytime measurements. For enhanced visibility, we smoothed
1261 FFC and $R_{obs}$ by a 5-day running average window. (C) Correlation of $R_{obs}$ and $R_{clear\ sky}$ versus
1262 fractional cloud cover. The linear fit is weighted by the occurrences (n) of cloud cover fractions and
1263 fixed to the origin (x=0, y=1). (D) Scatter plot of $R_{obs}$ and $R_{clear\ sky}$. (E) Scatter plot of $R_{obs}$ and corrected
1264 modeled solar radiation ($R_{model}$), which is based on $R_{clear\ sky}$ and FCC.

1265

1266

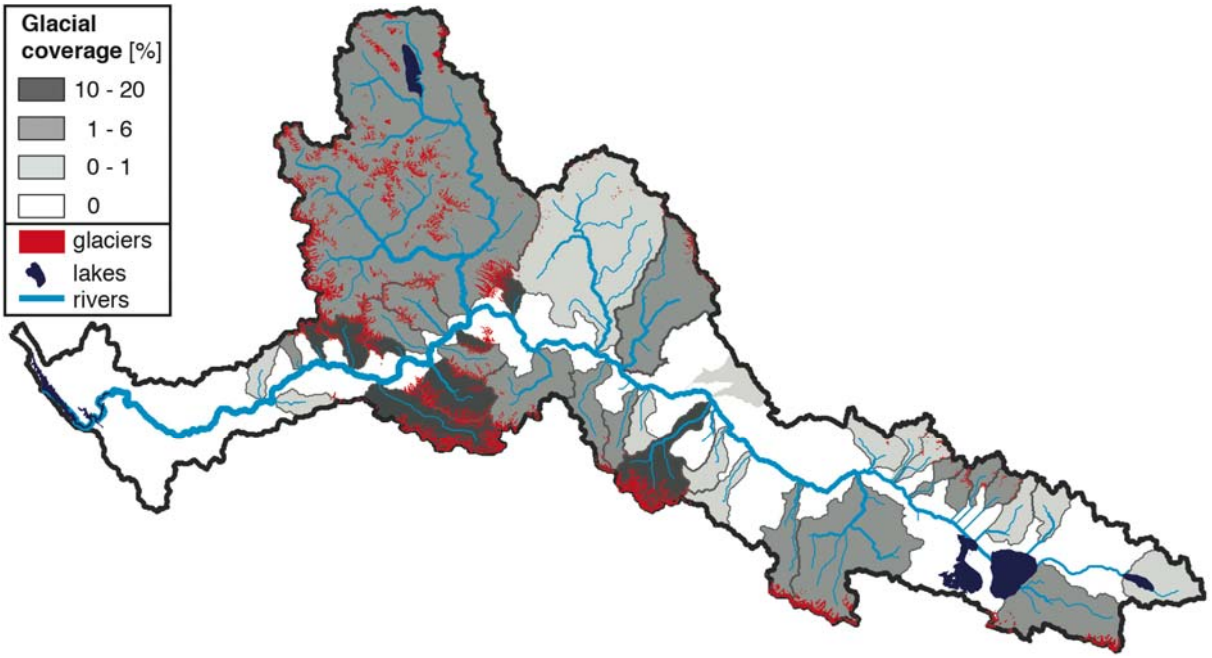


1267

1268 **Figure 9:** Glacial coverage for Sutlej tributary basins > 100 km$^2$ overlain by glacial extent, lakes, and
1269 rivers. Ice-coverage is based on *Frey et al.,* [2012]

1270

1271

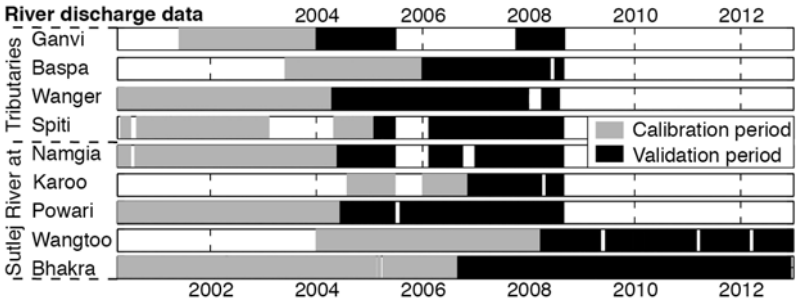


1272

1273 **Figure 10:** Overview of observed river discharge data at gauging stations of the Sutlej River and its
1274 tributaries (cf. Figure 1). We calibrate the hydrological model using the first data period (gray) and
1275 validated its performance based on the second data period (black).

1276

1277

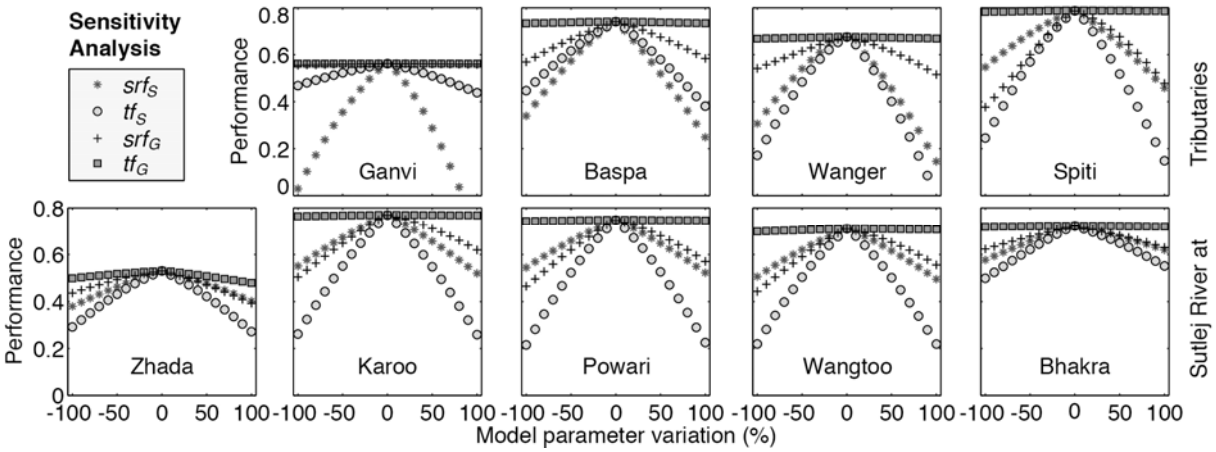


1278

1279 **Figure 11:** Sensitivity analysis of the shortwave radiation factors for snow- ($srf_S$) and glacier melt ($srf_G$)
1280 and the thermal factors for snow- ($tf_S$) and glacier melt ($tf_G$).

1281

1282

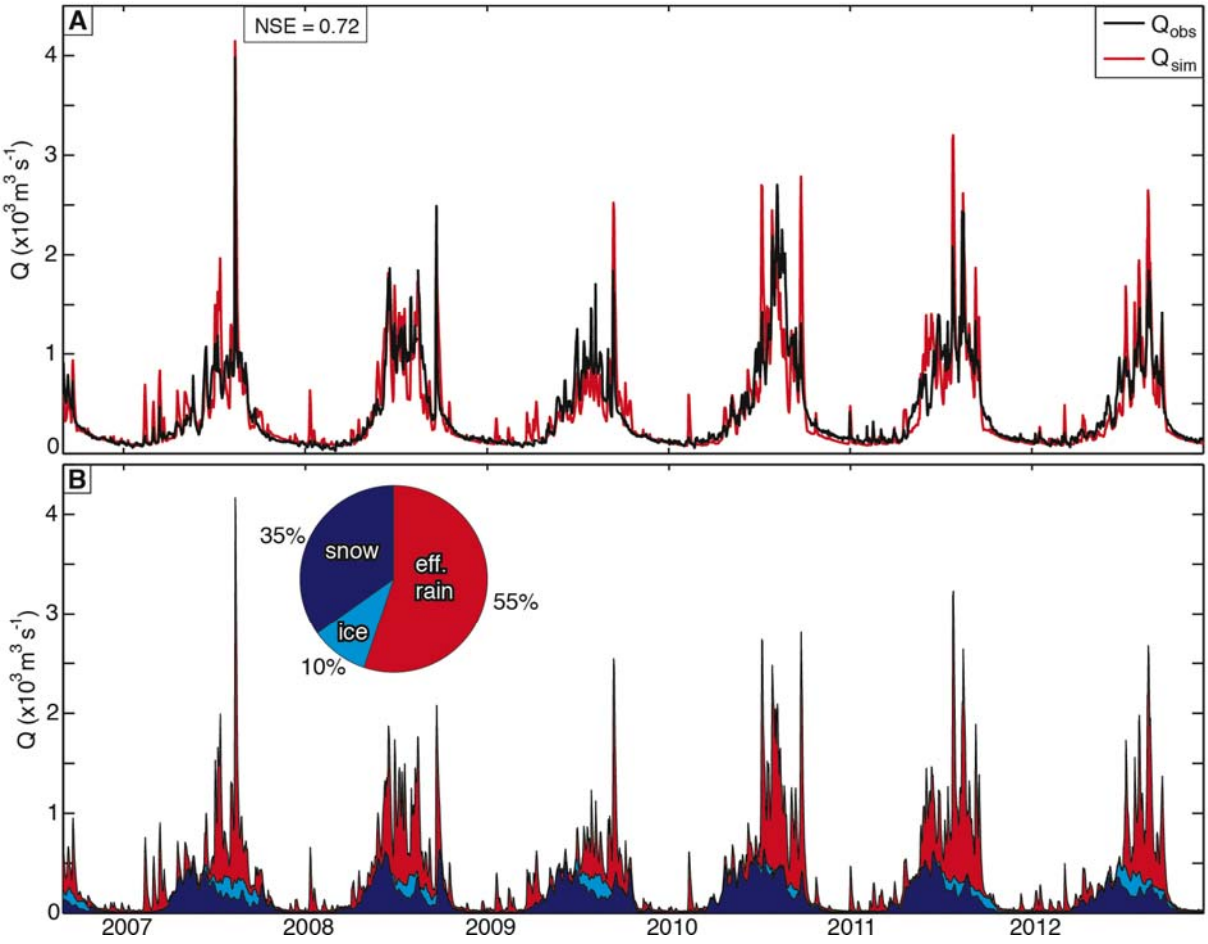


**Figure 12:** (A) Comparison of the observed and simulated daily discharges of the Sutlej River at Bhakra near the mountain front (cf. Figure 1) from September 2006 to December 2012. (B) Sum of the single simulated discharge components illustrating the different stacked contributions to total runoff. Pie chart represents the contribution of each runoff component to total discharge over the 6-year period.

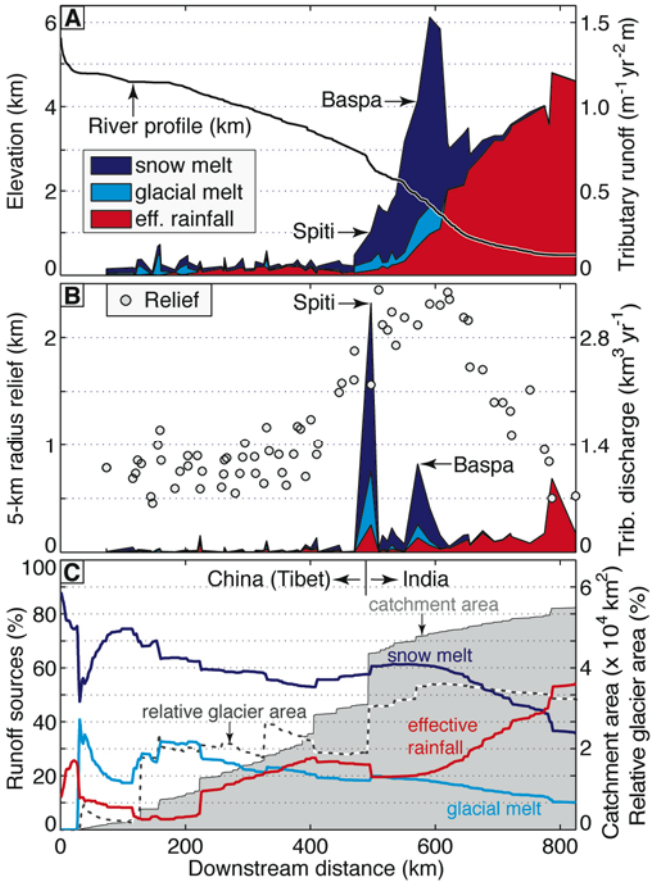


1291

1292 **Figure 13:** (A) Distance and elevation of the Sutlej longitudinal river profile along with stacked mean
1293 annual (2000-2012) runoff of tributaries > 100 km$^2$. (B) 5-km radius local relief and mean annual
1294 (2000-2012) river discharge of Sutlej River tributaries > 100 km$^2$. Color-coding is given in (A). (C)
1295 Runoff sources of the mean annual Sutlej river discharge along its river profile. Grey area indicated
1296 the catchment area along the downstream distance with relative glacier area indicated by the dash
1297 line.

1298

1299

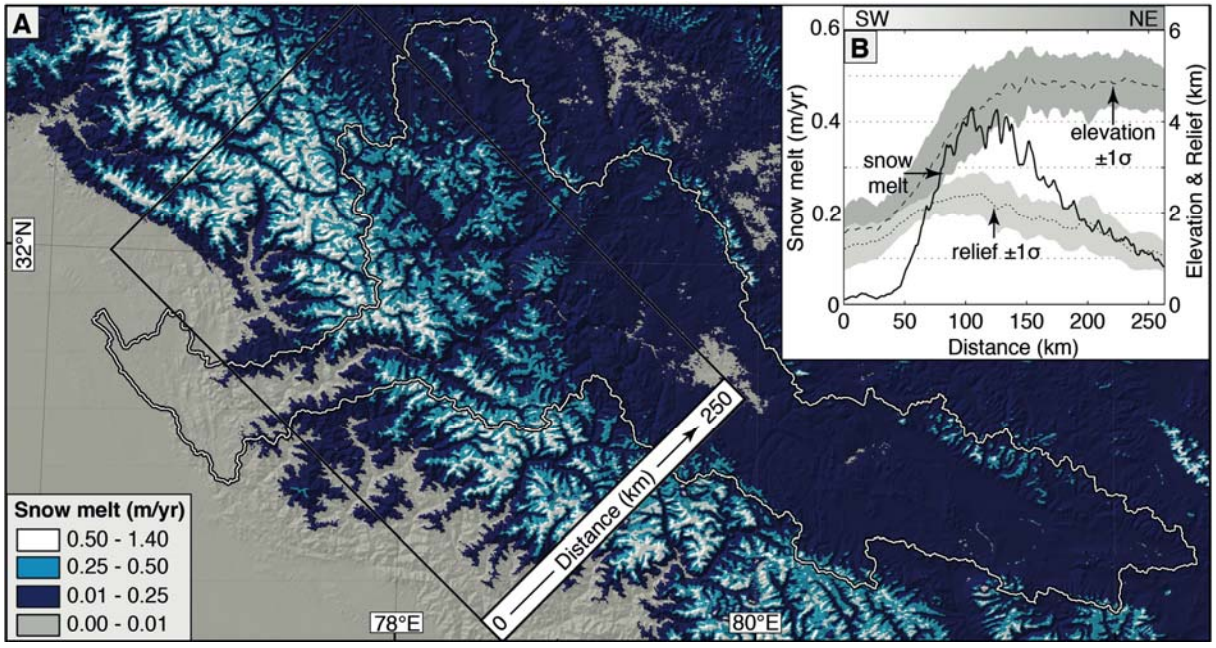


**Figure 14:** (A) Mean annual snow melt (October 2001 – September 2012) in the western Himalaya based on average snow melt factors of $srf_S$ = 0.04 mm $W^{-1}$ $m^2$ $day^{-1}$ and $tf_S$ = 2 mm $°C^{-1}$ $day^{-1}$ (B) 270-km wide swath profile across the western Himalaya showing the average distribution of snow melt along with elevation (±1σ) and a 5-km radius relief (±1σ).

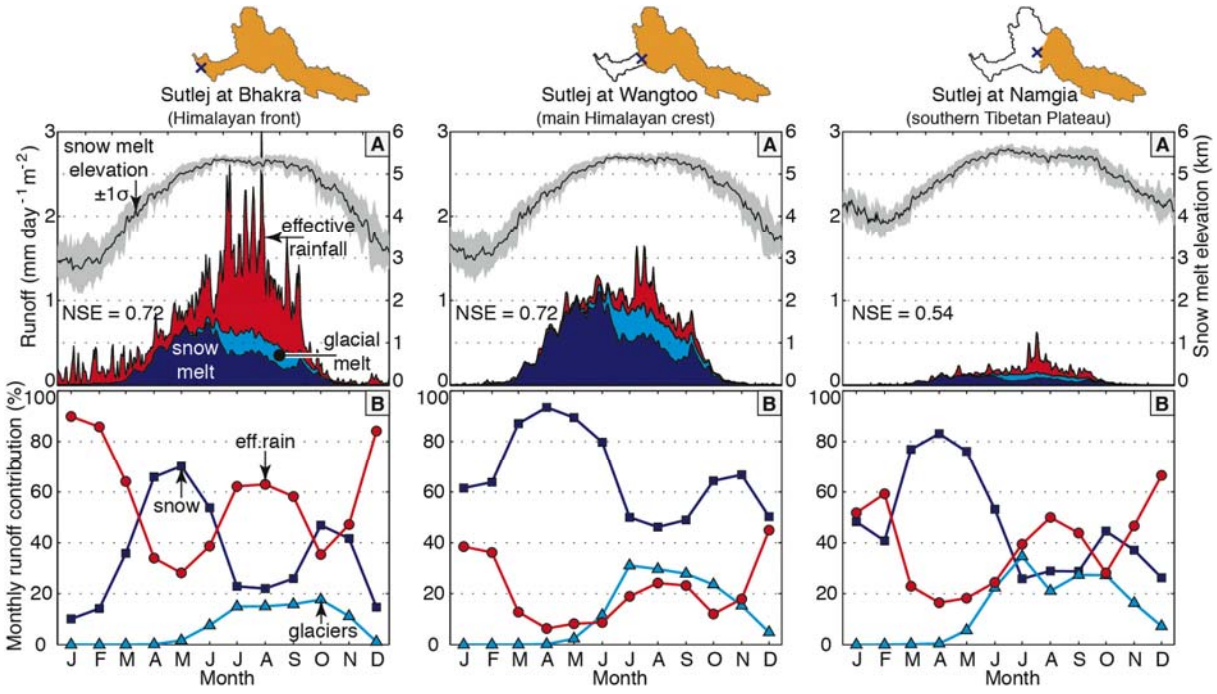


1307

1308 **Figure 15:** (A) Mean daily runoff of stacked hydrologic components for the Sutlej River (2000-2012) at
1309 Bhakra, Wangtoo and Namgia gauging stations (cf. Figure 1). Mean catchment-wide snow melt
1310 elevation (±1σ) increases to above 5000 m asl during the summer months. (B) Mean monthly
1311 percentages to total runoff as shown in A.

1312

1313

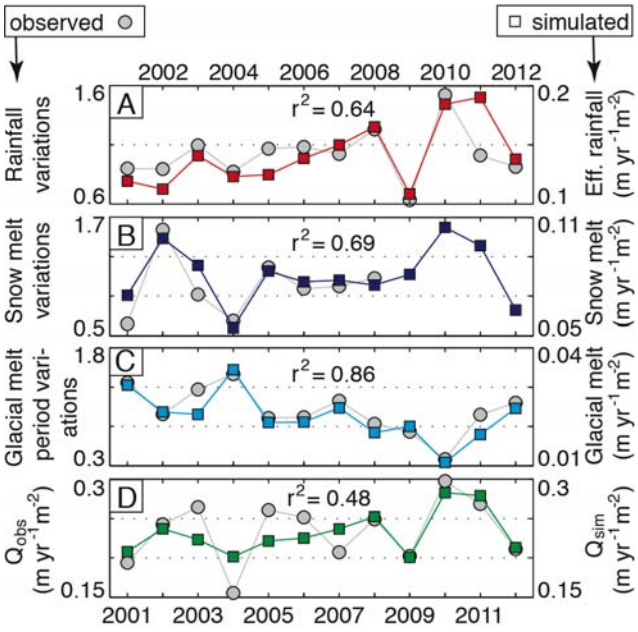


1314

1315 **Figure 16:** Comparison of inter-annual variations in observed and simulated hydrological components
1316 within the Sutlej Valley. (A) Normalized mean annual rainfall records of 23 weather stations versus the
1317 modeled mean annual runoff from effective rainfall. (B) Normalized mean annual SWE records of 15
1318 weather stations (2001-2008) versus the modeled mean annual snow melt runoff. (C) Normalized
1319 mean annual glacier melt period based on MODIS snow-cover data on glaciers versus modeled mean
1320 annual glacier melt runoff. (D) Observed river discharge versus modeled river discharge for the Sutlej
1321 River at Bhakra. The simulated runoff components in A, B, and C add up to the simulated river
1322 discharge in D.

1323

1324

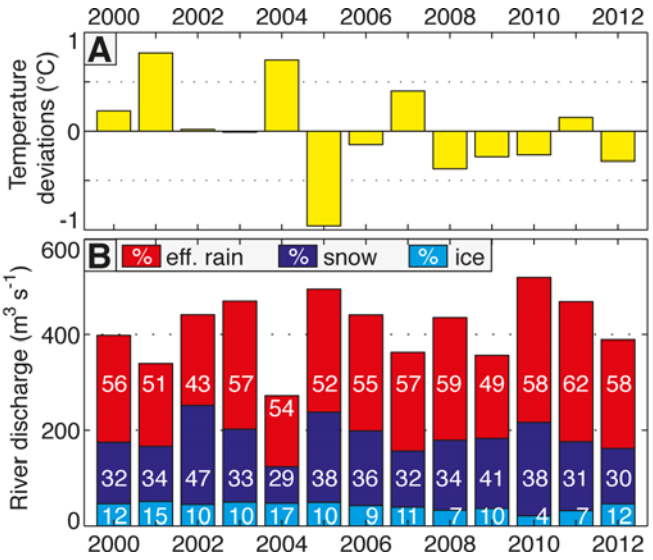


**Figure 17:** (A) Mean annual temperature deviations in Kalpa (Figure 1) from the average temperature of 10.44°C between 2000 and 2012. (B) Observed mean annual river discharge divided in its runoff components effective rainfall, snow melt, and glacier melt based on the hydrological modeling results for the Sutlej River at Bhakra. White numbers indicate the relative runoff contribution to the annual river discharge in %.

## Figure captions

**Figure 1:** (A) Shaded relief and elevation map of the western Himalaya with inset showing map location. Black polygon outlines the Sutlej catchment and defines the hydrologic model domain; white dashed line is the international border between India and China. White circles indicate weather stations recording rainfall and partially snow water equivalent. Gray squares represent weather stations in Patiala, Dehradun, Kalpa, Rakchham, Khab and Namgia (west to east), which additionally record daily minimum and maximum temperatures. Black stars denote river-gauging stations of the Sutlej main stem and tributaries at Bhakra (i), Ganvi (a), Wangtoo (h), Wanger (b), Baspa (c), Powari (g), Karoo (f), Spiti (d), Namgia (d) (west to east, cf. Table 1). (B) Characteristic ground-station data showing mean monthly temperature, precipitation, and runoff at the Himalayan Front (1), at the Himalayan Crest (2), and at the southern Tibetan Plateau (3).

**Figure 2:** Schematic overview of runoff fluxes and storage modules in the hydrological model. *SG1* and *SG2* represent fast and slow-leaking groundwater storages, respectively. $SI_{max}$, $SG1_{max}$, and $PERC_{max}$ represent thresholds for the generation of surface runoff, slow groundwater runoff, and the percolation rate (*PERC*), respectively.

**Figure 3:** (A) Flow-path distances in km for each cell to the Sutlej River at Bhakra. (B) Lag-time scaling factor based on the annual mean discharge at Bhakra smoothed with a 50-day running window. (C) Mean-seasonal flow path velocities for the path of each cell to the Sutlej River at Bahkra. Note the generally higher flow velocities in the steep sections of the middle Sutlej. (D) Mean-seasonal flow path times.

**Figure 4:** (A) Comparison of original (solid line), filtered (dotted line), and re-calibrated (dashed line) TRMM 3B42 V7 with weather station (WS) rainfall data at 66 locations below

2000 m asl for the time period 2000 to 2012. Scaling is based on the relation between TRMM 3B42 and weather station data (Figure 5) and TRMM 3B42 data is filtered for snow cover and maximum daily temperatures below 0°C. Mean annual rainfall in this region is >0.7 m/yr. (B) Comparison of original (solid line), filtered (dotted line), and filtered & scaled (dashed line) TRMM 3B42 (2000 to 2012) with snow water equivalent (SWE) and rainfall data of 16 weather stations (WS) located above 2000 m asl, where mean annual rainfall is <0.7 m/yr.

**Figure 5:** (A) Correlation of mean annual weather station (WS) rainfall data versus the ratio of mean annual TRMM 3B42 to WS data for the period 2000 to 2012. This rainfall ratio indicates a scaling factor by which TRMM over (>1) or underestimates (<1) weather station records. (B) Analysis of TRMM 3B42 data regarding its probability of detection and misinterpretation of daily rainfall at weather stations. (C) Topographic swath profile of the western Himalaya and the mean annual precipitation ratio of TRMM 3B42 and WS records. (D) Location of weather stations and the topographic swath profile.

**Figure 6:** Mean annual (2000 to 2012) distribution of snow covered area (SCA) and the percentage of misclassified snow on total snow cover (MOD10A1). We applied a 10-day moving average filter for enhanced visibility.

**Figure 7:** (A) Linear regression of daily maximum air temperatures from Kalpa, Rakchham, Namgia, Patiala, and Dehradun (cf. Figure 1) versus daytime MODIS Terra land surface temperatures (LST) weighted by the satellite sensor angle. In general, data with high residuals have higher sensor angles. (B) Same regression as in A for daily minimum temperatures versus nighttime MODIS Terra LST. Regressions for the MODIS Aqua sensor display the same trend (Figure S3). Nighttime correlation includes more data points as cloud cover at night is generally lower.

**Figure 8:** (A) Comparison of mean daily observed ($R_{obs}$) and computed ($R_{clear\ sky}$) incoming solar radiation from August 2006 to August 2008 at Khab (cf. Figure 1). (B) Fractional cloud cover (FCC) is derived from MODIS Aqua and Terra daytime measurements. For enhanced visibility, we smoothed FFC and $R_{obs}$ by a 5-day running average window. (C) Correlation of $R_{obs}$ and $R_{clear\ sky}$ versus fractional cloud cover. The linear fit is weighted by the occurrences (n) of cloud cover fractions and fixed to the origin (x=0, y=1). (D) Scatter plot of $R_{obs}$ and $R_{clear\ sky}$. (E) Scatter plot of $R_{obs}$ and corrected modeled solar radiation ($R_{model}$), which is based on $R_{clear\ sky}$ and FCC.

**Figure 9:** Glacial coverage for Sutlej tributary basins > 100 km$^2$ overlain by glacial extent, lakes, and rivers. Ice-coverage is based on *Frey et al.,* [2012]

**Figure 10:** Overview of observed river discharge data at gauging stations of the Sutlej River and its tributaries (cf. Figure 1). We calibrate the hydrological model using the first data period (gray) and validated its performance based on the second data period (black).

**Figure 11:** Sensitivity analysis of the shortwave radiation factors for snow- ($srf_S$) and glacier melt ($srf_G$) and the thermal factors for snow- ($tf_S$) and glacier melt ($tf_G$).

**Figure 12:** (A) Comparison of the observed and simulated daily discharges of the Sutlej River at Bhakra near the mountain front (cf. Figure 1) from September 2006 to December 2012. (B) Sum of the single simulated discharge components illustrating the different stacked contributions to total runoff. Pie chart represents the contribution of each runoff component to total discharge over the 6-year period.

**Figure 13:** (A) Distance and elevation of the Sutlej longitudinal river profile along with stacked mean annual (2000-2012) runoff of tributaries > 100 km$^2$. (B) 5-km radius local relief

and mean annual (2000-2012) river discharge of Sutlej River tributaries > 100 $km^2$. Color-coding is given in (A). (C) Runoff sources of the mean annual Sutlej river discharge along its river profile. Grey area indicated the catchment area along the downstream distance with relative glacier area indicated by the dash line.

**Figure 14:** (A) Mean annual snow melt (October 2001 – September 2012) in the western Himalaya based on average snow melt factors of $srf_s$ = 0.04 mm $W^{-1}$ $m^2$ $day^{-1}$ and $tf_s$ = 2 mm $°C^{-1}$ $day^{-1}$ (B) 270-km wide swath profile across the western Himalaya showing the average distribution of snow melt along with elevation (±1σ) and a 5-km radius relief (±1σ).

**Figure 15:** (A) Mean daily runoff of stacked hydrologic components for the Sutlej River (2000-2012) at Bhakra, Wangtoo and Namgia gauging stations (cf. Figure 1). Mean catchment-wide snow melt elevation (±1σ) increases to above 5000 m asl during the summer months. (B) Mean monthly percentages to total runoff as shown in A.

**Figure 16:** Comparison of inter-annual variations in observed and simulated hydrological components within the Sutlej Valley. (A) Normalized mean annual rainfall records of 23 weather stations versus the modeled mean annual runoff from effective rainfall. (B) Normalized mean annual SWE records of 15 weather stations (2001-2008) versus the modeled mean annual snow melt runoff. (C) Normalized mean annual glacier melt period based on MODIS snow-cover data on glaciers versus modeled mean annual glacier melt runoff. (D) Observed river discharge versus modeled river discharge for the Sutlej River at Bhakra. The simulated runoff components in A, B, and C add up to the simulated river discharge in D.

**Figure 17:** (A) Mean annual temperature deviations in Kalpa (Figure 1) from the average temperature of 10.44°C between 2000 and 2012. (B) Observed mean annual river discharge

1424 divided in its runoff components effective rainfall, snow melt, and glacier melt based on the
1425 hydrological modeling results for the Sutlej River at Bhakra. White numbers indicate the
1426 relative runoff contribution to the annual river discharge. White numbers indicate the relative
1427 runoff contribution to the annual river discharge in %.

1428

# Supporting Material

**Table S1**: Weather station details

| nb. | Weather station | Organi-sation | Latitude [°] | Lon-gitude [°] | Altitude [m] | Observation | Data period | Missing data [%] | Data length [days] |
|---|---|---|---|---|---|---|---|---|---|
| 1 | Sadar-Bilarspur | IMD | 31.348 | 76.762 | 576 | rainfall | 05.1999 - 11.2007 | 2.9 | 3136 |
| 2 | Ghumarwin | IMD | 31.436 | 76.708 | 640 | rainfall | 01.1998 - 12.2007 | 1.6 | 3652 |
| 3 | Jhanduta | IMD | 31.361 | 76.622 | 579 | rainfall | 01.2002 - 12.2007 | 0.0 | 2191 |
| 4 | Chamba | IMD | 32.558 | 76.126 | 963 | rainfall | 01.1998 - 02.2001 | 15.7 | 1155 |
| 5 | Chowari | IMD | 32.432 | 76.021 | 1079 | rainfall | 01.1998 - 02.2001 | 68.3 | 1155 |
| 6 | Bharmaur | IMD | 32.450 | 76.533 | 1867 | rainfall | 01.1998 - 10.2007 | 27.9 | 3591 |
| 7 | Churah(Tissa) | IMD | 32.833 | 76.167 | 1358 | rainfall | 11.1998 - 12.2007 | 7.3 | 3348 |
| 8 | Kalatop | IMD | 32.552 | 76.018 | 2376 | rainfall | 01.1998 - 12.2007 | 29.8 | 3652 |
| 9 | Holi | IMD | 32.364 | 76.521 | 1678 | rainfall | 01.1999 - 08.2007 | 70.2 | 3165 |
| 10 | Salooni | IMD | 32.728 | 76.034 | 1785 | rainfall | 07.2001 - 12.2007 | 2.5 | 2375 |
| 11 | Khajiyar | IMD | 32.546 | 76.059 | 1951 | rainfall | 07.2003 - 12.2007 | 7.3 | 1645 |
| 12 | Hamirpur | IMD | 31.684 | 76.519 | 763 | rainfall | 01.1998 - 12.2007 | 0.8 | 3652 |
| 13 | Bhoranj | IMD | 31.648 | 76.698 | 834 | rainfall | 01.1998 - 12.2007 | 0.8 | 3652 |
| 14 | Nadaun | IMD | 31.783 | 76.350 | 480 | rainfall | 01.1998 - 12.2007 | 0.8 | 3652 |
| 15 | Badsar | IMD | 31.543 | 76.450 | 757 | rainfall | 01.1998 - 07.1999 | 0.0 | 577 |
| 16 | Sujanpur | IMD | 31.832 | 76.503 | 557 | rainfall | 10.1998 - 12.2007 | 0.9 | 3379 |
| 17 | Dehra | IMD | 31.885 | 76.218 | 472 | rainfall | 12.1998 - 12.2007 | 35.0 | 3318 |
| 18 | Kangra | IMD | 32.103 | 76.271 | 1318 | rainfall | 01.1998 - 09.2006 | 5.6 | 3195 |
| 19 | Nurpur | IMD | 32.297 | 75.882 | 519 | rainfall | 01.1998 - 12.2007 | 3.3 | 3652 |
| 20 | Dharamshalla | IMD | 32.221 | 76.319 | 1385 | rainfall | 07.1998 - 12.2007 | 36.8 | 3471 |
| 21 | Palampur | IMD | 32.107 | 76.543 | 1281 | rainfall | 01.1998 - 12.2007 | 9.1 | 3652 |
| 22 | Jaswan Kotla | IMD | 32.237 | 76.046 | 518 | rainfall | 07.2002 - 12.2007 | 0.0 | 2010 |
| 23 | Shahpur | IMD | 32.226 | 76.170 | 807 | rainfall | 07.2003 - 02.2007 | 27.3 | 1339 |
| 24 | Nichar | BBMB | 31.552 | 77.976 | 2165 | rainfall | 01.1998 - 09.2008 | 6.2 | 3903 |
| 25 | Kilba | BBMB | 31.513 | 78.146 | 1935 | rainfall | 01.1998 - 09.2008 | 1.5 | 3902 |
| 26 | Sangla | BBMB | 31.430 | 78.266 | 2740 | rainfall | 02.2001 - 09.2008 | 6.6 | 2779 |
| 27 | Kalpa | BBMB | 31.544 | 78.255 | 2731 | rainfall | 01.1998 - 10.2008 | 0.7 | 3953 |
| 28 | Pooh | BBMB | 31.763 | 78.589 | 2699 | rainfall | 11.1999 - 12.2007 | 6.0 | 2983 |
| 29 | Banjar | IMD | 31.637 | 77.344 | 1427 | rainfall | 01.1998 - 12.2007 | 2.5 | 3652 |
| 30 | Keylong | IMD | 32.567 | 77.044 | 3048 | rainfall | 01.1998 - 12.2007 | 33.4 | 3652 |
| 31 | Kaza | BBMB | 32.176 | 78.104 | 3541 | rainfall | 01.1998 - 04.2008 | 25.7 | 3773 |
| 32 | Udaipur | IMD | 32.725 | 76.663 | 2649 | rainfall | 10.1998 - 06.2006 | 1.0 | 2830 |
| 33 | Sadar-Mandi | IMD | 31.712 | 76.933 | 761 | rainfall | 01.1998 - 12.2007 | 0.8 | 3652 |
| 34 | Jogindernagar | IMD | 32.036 | 76.734 | 1442 | rainfall | 01.1998 - 12.2007 | 0.8 | 3652 |
| 35 | Sarkaghat | IMD | 31.704 | 76.812 | 1155 | rainfall | 01.1998 - 12.2007 | 0.8 | 3652 |
| 36 | Chachiot | IMD | 31.550 | 77.017 | 1529 | rainfall | 09.2000 - 12.2007 | 0.0 | 2678 |
| 37 | Sundernagar | IMD | 31.534 | 76.905 | 889 | rainfall | 01.1998 - 01.2007 | 0.9 | 3318 |
| 38 | Karsog | IMD | 31.383 | 77.200 | 1417 | rainfall | 01.1998 - 12.2007 | 0.8 | 3652 |
| 39 | Sandhol | IMD | 31.881 | 76.678 | 651 | rainfall | 03.1998 - 12.2007 | 2.4 | 3593 |
| 40 | Bharol | IMD | 31.936 | 76.699 | 644 | rainfall | 01.1999 - 12.2007 | 0.9 | 3287 |
| 41 | Baldwara | IMD | 31.529 | 76.736 | 764 | rainfall | 06.2004 - 12.2007 | 0.0 | 1309 |
| 42 | Rampur | IMD | 31.452 | 77.633 | 972 | rainfall | 01.1998 - 12.2007 | 0.8 | 3652 |
| 43 | Rohru | IMD | 31.204 | 77.751 | 1565 | rainfall | 01.1998 - 12.2007 | 5.8 | 3652 |

| nb. | Weather station | Organi-sation | Latitude [°] | Lon-gitude [°] | Altitude [m] | Observation | Data period | Missing data [%] | Data length [days] |
|---|---|---|---|---|---|---|---|---|---|
| 44 | Jubbal | IMD | 31.120 | 77.670 | 2145 | rainfall | 08.1998 - 02.2007 | 19.4 | 3134 |
| 45 | Chopal | IMD | 30.950 | 77.583 | 2311 | rainfall | 01.1998 - 01.2007 | 87.2 | 3318 |
| 46 | Theog | IMD | 31.124 | 77.347 | 2101 | rainfall | 01.1998 - 01.2007 | 4.6 | 3318 |
| 47 | Kumarsain | IMD | 31.317 | 77.450 | 1617 | rainfall | 01.1998 - 10.2006 | 1.9 | 3226 |
| 48 | Suni | IMD | 31.230 | 77.164 | 765 | rainfall | 01.1998 - 12.2007 | 1.6 | 3652 |
| 49 | Kothai | IMD | 31.119 | 77.485 | 1531 | rainfall | 01.1998 - 07.2007 | 8.7 | 3499 |
| 50 | Dodrakwar | IMD | 31.209 | 78.070 | 2364 | rainfall | 01.1999 - 04.2007 | 65.8 | 3042 |
| 51 | Mashobra | IMD | 31.130 | 77.229 | 2240 | rainfall | 01.1998 - 12.2007 | 3.3 | 3652 |
| 52 | Chiragaown | IMD | 31.238 | 77.899 | 1844 | rainfall | 11.2001 - 12.2007 | 12.3 | 2252 |
| 53 | Kupvi | IMD | 30.816 | 77.424 | 2165 | rainfall | 01.2002 - 12.2007 | 9.8 | 2191 |
| 54 | Nahan | IMD | 30.559 | 77.289 | 874 | rainfall | 11.1999 - 12.2007 | 1.4 | 2983 |
| 55 | Paonta Sahib | IMD | 30.470 | 77.625 | 433 | rainfall | 01.1998 - 12.2007 | 17.1 | 3652 |
| 56 | Rakuna | IMD | 30.605 | 77.473 | 688 | rainfall | 01.1998 - 12.2007 | 2.0 | 3652 |
| 57 | Pachhad | IMD | 30.777 | 77.164 | 1257 | rainfall | 09.1999 - 12.2007 | 0.4 | 3044 |
| 58 | Dadahu | IMD | 30.599 | 77.437 | 635 | rainfall | 01.1998 - 12.2007 | 2.0 | 3652 |
| 59 | Dhaula Kuan | IMD | 30.517 | 77.479 | 443 | rainfall | 01.1998 - 12.2007 | 4.5 | 3652 |
| 60 | Nohradhar | IMD | 30.813 | 77.473 | 2558 | rainfall | 07.2002 - 01.2007 | 87.2 | 1676 |
| 61 | Rajgarh | IMD | 30.850 | 77.300 | 1567 | rainfall | 09.2003 - 12.2007 | 0.0 | 1583 |
| 62 | Kandaghat | IMD | 30.965 | 77.119 | 1339 | rainfall | 01.1998 - 12.2007 | 35.0 | 3652 |
| 63 | Kasauli | IMD | 30.901 | 76.963 | 1820 | rainfall | 01.1998 - 12.2007 | 0.3 | 3652 |
| 64 | Nalagarh | IMD | 31.042 | 76.719 | 386 | rainfall | 01.1998 - 12.2007 | 50.3 | 3652 |
| 65 | Arki | IMD | 31.154 | 76.964 | 1176 | rainfall | 06.1998 - 12.2007 | 0.3 | 3501 |
| 66 | Nauni | IMD | 30.900 | 77.224 | 933 | rainfall | 07.2003 - 12.2007 | 1.9 | 1645 |
| 67 | Una | IMD | 31.473 | 76.314 | 424 | rainfall | 01.1998 - 12.2007 | 1.2 | 3652 |
| 68 | Amb | IMD | 31.686 | 76.116 | 477 | rainfall | 07.2000 - 12.2007 | 1.5 | 2740 |
| 69 | Bangana | IMD | 31.649 | 76.382 | 610 | rainfall | 01.1998 - 12.2007 | 35.0 | 3652 |
| 70 | Bahli | BBMB | 31.371 | 77.647 | 2298 | rainfall, SWE | 07.2001 - 09.2008 | 5.9 | 2631 |
| 71 | Chhitkul | BBMB | 31.353 | 78.436 | 3448 | rainfall, SWE | 04.2001 - 08.2008 | 0.1 | 2710 |
| 72 | Giabong | BBMB | 31.779 | 78.443 | 2936 | rainfall, SWE | 11.2001 - 04.2008 | 23.2 | 2373 |
| 73 | Losar | BBMB | 32.438 | 77.750 | 4099 | rainfall, SWE | 01.2006 - 12.2007 | 46.2 | 730 |
| 74 | Malling | BBMB | 31.894 | 78.627 | 3561 | rainfall, SWE | 11.2001 - 08.2008 | 28.1 | 2496 |
| 75 | Moorang | BBMB | 31.591 | 78.448 | 2514 | rainfall, SWE | 10.1999 - 08.2008 | 0.9 | 3258 |
| 76 | Namgia | BBMB | 31.810 | 78.656 | 2843 | rainfall, SWE | 12.2003 - 08.2008 | 0.0 | 1736 |
| 77 | Narkandar | BBMB | 31.257 | 77.459 | 2709 | rainfall, SWE | 07.2001 - 02.2008 | 21.5 | 2435 |
| 78 | Purbani | BBMB | 31.589 | 78.308 | 2508 | rainfall, SWE | 08.2001 - 09.2008 | 0.0 | 2598 |
| 79 | Rakchham | BBMB | 31.392 | 78.354 | 3131 | rainfall, SWE | 01.2005 - 08.2008 | 0.1 | 1338 |
| 80 | Sarahan | BBMB | 31.509 | 77.793 | 2146 | rainfall, SWE | 12.2001 - 02.2008 | 8.1 | 2262 |
| 81 | Khab | BBMB | 31.763 | 78.637 | 2519 | rainfall, SWE, radiation | 08.2006 - 08.2008 | 10.1 | 755 |
| 82 | Ngari | WMO | 32.501 | 80.105 | 4279 | rainfall, SWE | 06.2004 - 12.2012 | 0.0 | 3136 |
| 83 | Dehradun | WMO | 30.317 | 78.032 | 683 | rainfall, SWE | 06.2004 - 12.2012 | 0.0 | 3136 |
| 84 | Patiala | WMO | 30.320 | 76.395 | 251 | rainfall, SWE | 06.2004 - 12.2012 | 0.0 | 3136 |

**Table S2**: Parameters of solar radiation module

| *Solar radiation module* | | |
|---|---|---|
| **Parameter** | **Unit** | **Value** |
| Solar Constant | W / m² | 1367 |
| Time Span | h | 0-24 |
| Time Resolution | h | 0.25 |
| Lumped Atmospheric Transmittance | Percent | 60 |
| Height of Atmosphere | km | 10 |
| Water Vapour Pressure | mbar | 10 |
| Athmospheric Pressure | mbar | 1013 |
| Water Content | cm | 1.68 |
| Dust | ppm | 100 |

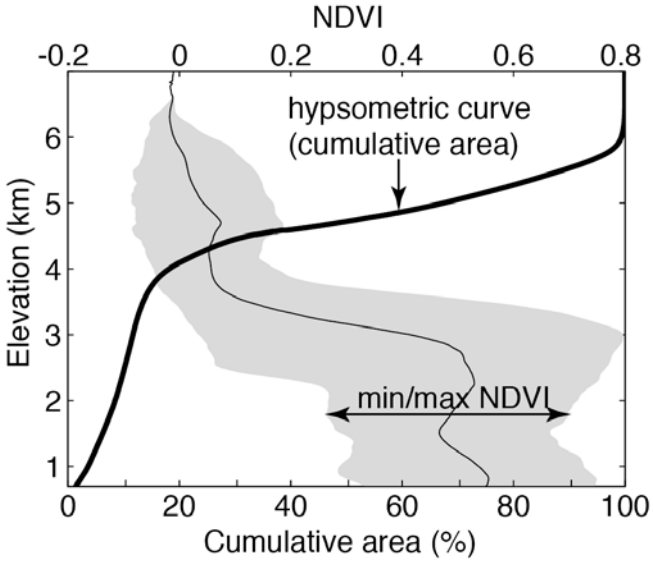


1440

1441 **Figure S1:** Hypsometry of the Sutlej River catchment and its vegetation distribution illustrated by the
1442 Normalized Difference Vegetation Index (NDVI) based on MODIS vegetation data. Note that the vast
1443 majority of the catchment is situated at elevations above 3.5 km asl displaying no vegetation cover.

1444

1445

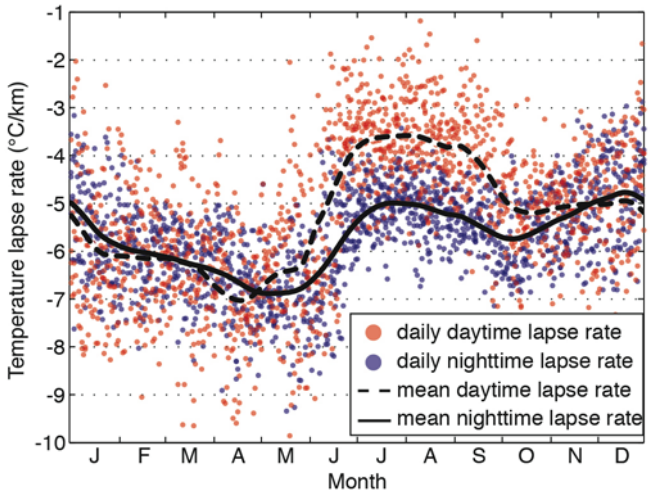


1446

1447 **Figure S2:** Mean daily atmospheric lapse rate in the Sutlej Valley based on weather station data from
1448 Patiala, Dehradun, Kalpa, Rakchham, and Namgia. Data displays daily lapse rate of each Julian day
1449 during the period June 2004 to August 2008 (n=1553). The dashed and solid black lines represent the
1450 mean daily atmospheric lapse rate for the day and nighttime, respectively, which we used to
1451 extrapolate daily air temperatures from Kalpa.

1452

1453

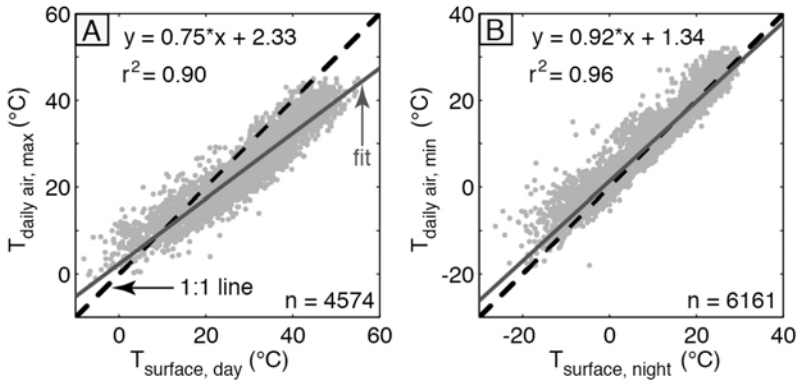


1454

1455 **Figure S3:** (A) Linear regression of daily maximum air temperatures from Kalpa, Rakchham, Namgia,
1456 Patiala, and Dehradun (cf. Figure 1) versus daytime MODIS Aqua land surface temperatures (LST)
1457 weighted by the satellite sensor angle. In general, data with high residuals have higher sensor angles.
1458 (B) Same regression as in A for daily minimum temperatures versus nighttime MODIS Terra LST.
1459 Nighttime correlation includes more data points as cloud cover at night is generally lower.

1460

1461

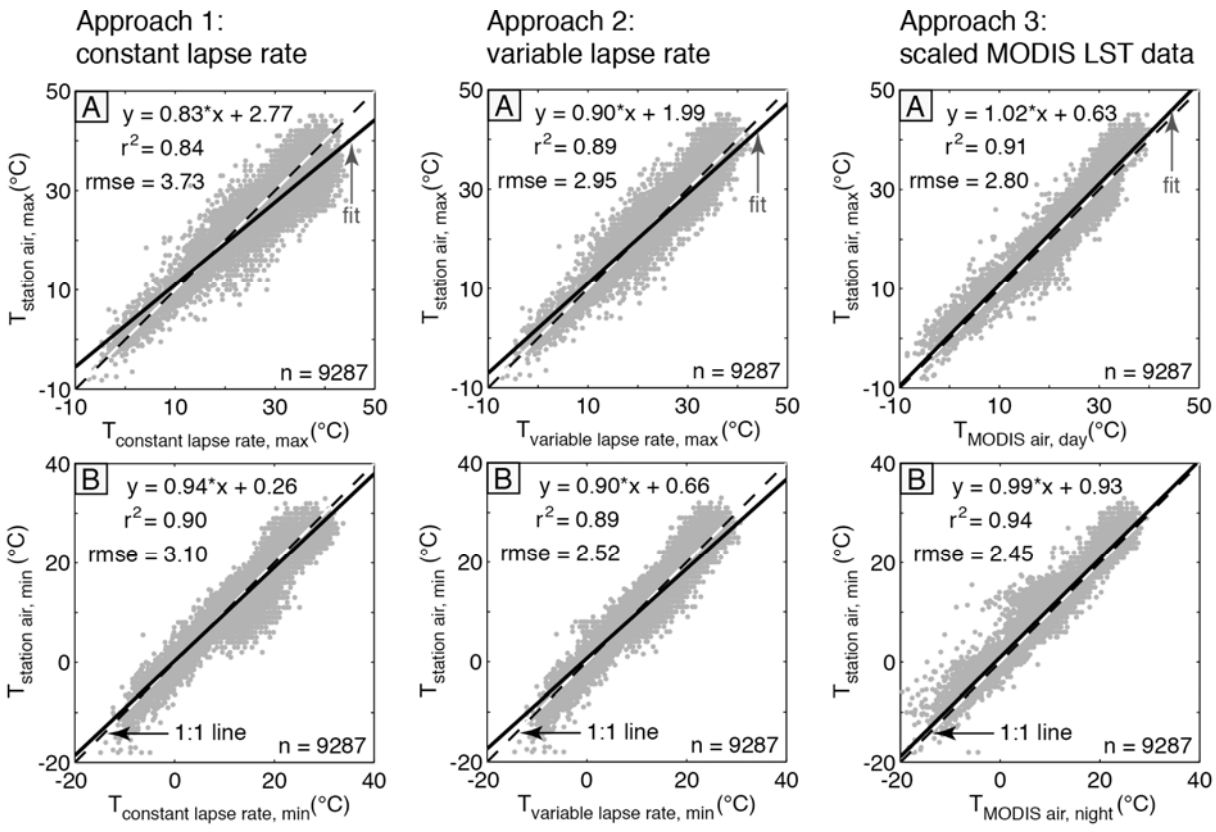


**Figure S4:** Evaluation of modeled temperatures by approaches 1, 2, and 3 based on regressions with weather station data. (A) Linear regression of daily maximum air temperatures from Rakchham, Namgia, Patiala, and Dehradun (cf. Figure 1) versus extrapolated maximum air temperatures from Kalpa based on a constant atmospheric lapse rate of -6.5°C/km (approach 1), seasonally varying atmospheric lapse rate (approach 2), and scaled MODIS Terra daytime temperatures (approach 3). (B) Same regression as in A for daily minimum temperatures.

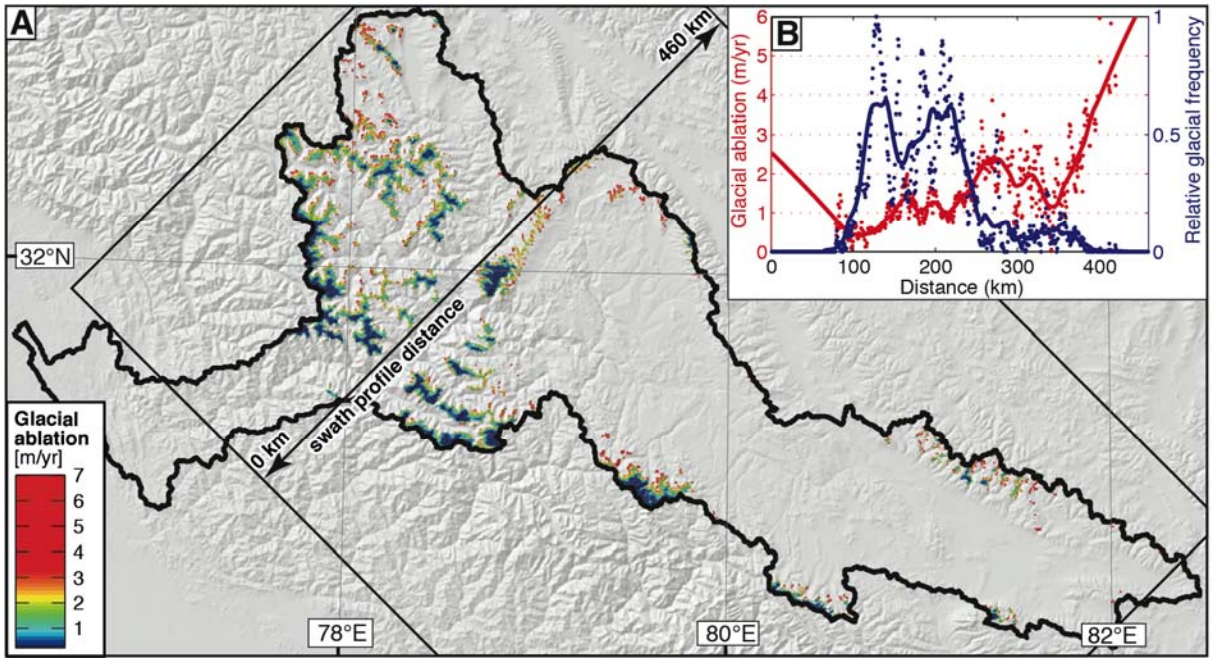


1471

1472 **Figure S5:** (A) Mean annual glacier melt (January 2001 – December 2012) in the western Himalaya
1473 based on calibrated glacier melt factors for the Sutlej River at Bhakra of $srf_g$ = 0.12 mm $W^{-1}$ $m^2$ $day^{-1}$
1474 and $tf_g$ = 0.38 mm $°C^{-1}$ $day^{-1}$. (B) Swath profile across the western Himalaya showing the average
1475 distribution of glacier melt along with the frequency distribution of glacial cells. Both bold lines
1476 represent a 50 data points running average window.

1477

1478

1479 **Table 3:** Evaluation of air temperature datasets based on linear regressions with weather-
1480 station records

| Approach | Method | Regression parameter | | | | | |
|---|---|---|---|---|---|---|---|
| | | $r^2$ | | *rmse* [°C] | | *fit slope* | |
| [#] | | day | night | day | night | day | night |
| 1 | Seasonally constant lapse rate (-6.5°C/km) | 0.84 | 0.90 | 3.72 | 3.10 | 0.83 | 0.94 |
| 2 | Seasonally variable day- and night lapse rate | 0.89 | 0.92 | 2.95 | 2.51 | 0.90 | 0.90 |
| 3 | Scaled MODIS LST data | 0.91 | 0.94 | 2.80 | 2.45 | 1.02 | 0.99 |

1481

1482

1483

1484 **Table 4:** Tunable and constant parameters of the melt and runoff response routine

| Parameter | Description | Unit | Range[a] | Value[a] | Estimation method |
|---|---|---|---|---|---|
| *Snow and glacier routine* | | | | | |
| $srf_S$ | shortwave radiation factor for snow melt | [mm $W^{-1}$ $m^2$ $day^{-1}$] | 0 - 0.129 | 0.019 | Calibration |
| $tf_S$ | empirical temperature factor for snow melt | [mm $°C^{-1}$ $day^{-1}$] | 0 - 7.75 | 1.80 | Calibration |
| $srf_G$ | shortwave radiation factor for glacial melt | [mm $W^{-1}$ $m^2$ $day^{-1}$] | 0 - 0.645 | 0.119 | Calibration |
| $tf_G$ | empirical temperature factor for glacial melt | [mm $°C^{-1}$ $day^{-1}$] | 0 - 32.28 | 0.38 | Calibration |
| *df* | Scaling factor for debris-covered ice | [dimensionless] | - | 0.7 | Azam et al. 2012[b] |
| $T_T$ | Threshold temperature | [°C] | - | 0 | Viviroli et al. 2007[c] |
| *Runoff response routine* | | | | | |
| $SI_{MAX}$ | Threshold content of the lower SUZ for generation of surface runoff (SGR) | [mm] | 0-1000 | 158.7 | Calibration |
| $SG1_{MAX}$ | Threshold content of the SG1 for generation of slow-leaking recharge | [mm] | 0-1000 | 794.8 | Calibration |
| $PERC_{MAX}$ | Maximal deep percolation rate | [mm $day^{-1}$] | 0-1000 | 232.0 | Calibration |
| *K0* | Storage time for surface runoff | [day] | - | 0.42 | Viviroli et al. 2007[c] |
| *K1* | Storage time for interflow | [day] | - | 3.13 | Viviroli et al. 2007[c] |
| *K2* | Storage time for quick groundwater flow | [day] | - | 31.25 | Viviroli et al. 2007[c] |
| *K3* | Storage time for slow groundwater flow | [day] | - | 104.16 | Viviroli et al. 2007[c] |

1485

1486 [a] Range and value of tunable parameters are given exemplarily for the Sutlej catchment at
1487 Bhakra.

1488 [b] value is based on mass balance data published by *Azam et al.*, [2012]

1489 [c] use of PREVAH-default values for the respective runoff type storage time as defined in
1490 *Viviroli et al.* [2007]

1491

**Table 5:** Comparison of our three different rainfall dataset by their Nash Sutcliffe Efficiency (NSE), relative volume error (RVE), and their mean annual catchment rainfall (Rain).

| *Rainfall datasets:* | | (1) Weather station data | | | (2) TRMM original | | | (3) TRMM re-calibrated | | | (3) Discharge sources[a] | | |
|---|---|---|---|---|---|---|---|---|---|---|---|---|---|
| | | NSE | RVE | Rain | NSE | RVE | Rain | NSE | RVE | Rain | Snow | Ice | Rain-ET |
| **Catchments** | | [-] | [%] | [mm/yr] | [-] | [%] | [mm/yr] | [-] | [%] | [mm/yr] | [%] | [%] | [%] |
| *Tributaries* | Ganvi (a) | 0.50 | -5.9 | 494 | 0.27 | 21.8 | 745 | 0.59 | 1.4 | 511 | 58 | 1 | 41 |
| | Wanger (b) | 0.55 | -2.6 | 245 | 0.54 | 12.3 | 478 | 0.68 | -2.3 | 162 | 72 | 15 | 13 |
| | Baspa (c) | 0.77 | 9.3 | 266 | 0.56 | 15.6 | 514 | 0.75 | -6.5 | 218 | 75 | 13 | 13 |
| | Spiti (d) | -7.49 | 123.6 | 273 | -0.16 | 39.0 | 152 | 0.78 | -0.2 | 31 | 67 | 22 | 11 |
| *Sutlej River at* | Namgia (e) | -107.91 | 531.8 | 392 | -36.81 | 309.9 | 237 | 0.54 | -1.6 | 50 | 42 | 19 | 39 |
| | Karoo (f) | -6.30 | 135.4 | 351 | -2.90 | 100.2 | 213 | 0.71 | 2.8 | 44 | 65 | 18 | 17 |
| | Powari (g) | -18.22 | 194.2 | 350 | -3.17 | 98.9 | 213 | 0.75 | -2.2 | 45 | 66 | 17 | 18 |
| | Wangtoo (h) | -2.60 | 99.7 | 348 | -3.16 | 84.1 | 218 | 0.72 | -3.2 | 51 | 66 | 18 | 16 |
| | Bhakra (i) | -5.24 | 96.1 | 392 | -1.99 | 68.4 | 300 | 0.72 | 1.1 | 131 | 35 | 10 | 55 |

[a] The discharge sources represent the modeling results for the third re-calibrated TRMM rainfall dataset, which we used to drive the hydrological model.